DOI: https://doi.org/10.2138/am-2022-8823. http://www.minsocam.org/

Revision 1 of 8823

Nature and timing of Sn mineralization in southern Hunan, South China: Constraints from LA-ICP-MS cassiterite U-Pb geochronology and trace element composition

Tao Ren[a], Huan Li[a]*, Thomas J. Algeo[b, c, d], Musa Bala Girei[e], Jinghua Wu[a], Biao Liu[a]

[a] *Key Laboratory of Metallogenic Prediction of Nonferrous Metals and Geological Environment Monitoring, Ministry of Education, School of Geosciences and Info–Physics, Central South University, Changsha 410083, China*

[b] *State Key Laboratory of Geological Processes and Mineral Resources, School of Earth Resources, China University of Geosciences, Wuhan 430074, China*

[c] *State Key Laboratory of Biogeology and Environmental Geology, School of Earth Sciences, China University of Geosciences, Wuhan 430074, China*

[d] *Department of Geosciences, University of Cincinnati, Cincinnati, OH 42221-0013 USA*

[e] *Department of Geology, Bayero University Kano, Kano State, Nigeria*

*Corresponding author (H. Li): lihuan@csu.edu.cn

ABSTRACT

Accurately determining the timing and mechanism of metallogenesis of ore deposits is essential for developing a robust genetic model for their exploration. In this paper, we analyze the formation conditions of cassiterite in five major deposits of southern Hunan Province, one of the most important tungsten-tin (W-Sn) provinces in South

China, using a combination of cathodoluminescence imaging, in situ U-Pb geochronology, and trace-element concentration data. In situ cassiterite U-Pb geochronology constrains the main period of Sn mineralization to between 155.4 and 142.0 Ma, demonstrating a temporal and genetic relationship to silicic intrusive magmatism in the same area. Three stages of magmatic activity and metallogenic evolution are recognized: (1) Early Paleozoic and Triassic: the initial enrichment stage of tungsten and tin; (2) Jurassic: the metasomatic mineralization stage; and (3) Cretaceous: the magmatic-hydrothermal superposition stage. The cassiterite in these deposits takes four forms, i.e., quartz vein-type, greisen-skarn-type, greisen-type, and granite-type, representing a progression characterized by the increasing content and decreasing range of variation of high-field-strength elements (HFSEs), and reflecting a general increase in the degree of evolution of the associated granites. Rare earth element (REE) concentrations suggest that precipitation of cassiterite was insensitive to the redox state of the fluid, and that precipitation of cassiterite in the southern Hunan Sn deposits did not require a high-fO_2 environment. These findings provide new insights into tin mineralization processes and exploration strategies.

Keywords: tin; tungsten; U-Pb dating; geochemistry; metallogenesis; Nanling

INTRODUCTION

Cassiterite (SnO_2), the most economically important tin (Sn)-bearing mineral, is generally mined from primary magmatic-hydrothermal deposits that are spatially and temporally associated with highly differentiated granites (Heinrich 1990; Cheng et al. 2019; Zhu et al. 2021). Accurately determining the timing and duration of precipitation of cassiterite is essential to understanding Sn-ore mineralization processes and thus generating genetic models that can aid in prospecting for rare large tin deposits (Yuan et al. 2018). Given its tetragonal, rutile-type structure, cassiterite typically has a high U-Pb ratio as well as a high closure temperature (Zhang et al. 2011, 2017; Neymark et al. 2018). These characteristics give it high resistance to post-ore hydrothermal alteration (Plimer et al. 1991; Hu et al. 2021). Due to their similarities to Sn^{4+} with respect to ionic charges, radii, and coordination numbers, trace elements such as Hf, Zr, Sc, Ta, Nb, Ti, Fe, Mn, In, U and W are able to substitute for Sn in cassiterite either directly or through a coupled substitution mechanism. These elements can be used to trace the cassiterite growth environment as well as the source of mineralizing fluids (Schmidt 2018; Cheng et al. 2019; Bennett et al. 2020; Lehmann et al. 2021; Wu et al. 2021).

The southern Hunan Province, located within the western Nanling metallogenic belt, is one of the most important W-Sn metallogenic regions in China (Mao et al. 2007; Hu et al. 2017; Jiang et al. 2020). This province consists of several major Sn-polymetallic deposits including the Hehuaping, Bailashui, and Xitian deposits (SnO_2 reserves of 140 metric kilotons [Kt], 420 Kt, and 178 Kt respectively; Yao et al. 2014; Wang et al. 2014; Li et al. 2019). Also located within this province are the Dengfuxian (quartz vein-type), Dayishan (greisen-type), Shizhuyuan (greisen-skarn-type), Xianghualing (granite-type), and Jiuyishan (greisen-type) deposits that are the focus of this study. These deposits are spatially and temporally related to highly differentiated granites of mid-Mesozoic (165-150 Ma) age that have experienced pervasive hydrothermal alteration (Sun et al. 2018; Li et al. 2018a, b; Yang et al. 2018; Xiong et al. 2020; Liao et al. 2021; Wu et al. 2021, Zhu et al. 2021). Despite extensive geochronological research, the relative timings of magma emplacement and Sn-polymetallic mineralization in this province are still poorly known—partly because earlier studies used conventional radiometric dating systems that are readily disturbed in mineralized granite systems (e.g., mica Ar-Ar) (Yin et al. 2002; Cai et al. 2012; Wu et al. 2018; Liu et al. 2019; Liao et al. 2021), and partly because few studies analyzed cassiterite to establish constraints on the timing of tin mineralization. Here, we address this issue by providing new U-Pb dates (i.e., for the Dengfuxian Dayishan, and Xianghualing deposits) as well as the first U-Pb ages for cassiterite (i.e., for the Shizhuyuan and Jiuyishan deposits) for these deposits. Moreover, differences in initial fluid composition and fluid evolution between various types of tin deposits are not clear owing to a paucity of geochemical studies targeting the main tin-bearing phase (i.e., cassiterite).

In this contribution, we undertook a study of cassiterite in five major W-Sn deposits of southern Hunan Province, using a combination of cathodoluminescence, LA-ICP-MS U-Pb ages, and trace-element concentrations. Our objectives were: (1) to better constrain the timing of Sn-polymetallic mineralization; (2) to determine genetic links between Sn-polymetallic mineralization and the associated granitic rocks; and (3) to constraint differences in geochemical characteristics and evolution of ore-forming fluids among the different types of Sn deposits by analyzing cassiterite trace-element compositions.

REGIONAL GEOLOGY

The South China Craton is composed of the Yangtze Block and the Cathaysia Block, sutured along the Pingxiang-Jiangshan-Shaoxing Fault Zone (Fig. 1a and 1b; Li and McCulloch 1996; Zhang et al. 2017). These two blocks were amalgamated during the mid-Neoproterozoic Jiangnan Orogeny (Zhang et al. 2017; Song et al. 2020). The South China Craton experienced multiple tectonic events between the Early Paleozoic and Mesozoic, triggering the emplacement of numerous magmatic rocks that are associated with economically significant hydrothermal W-Sn ore

DOI: https://doi.org/10.2138/am-2022-8823. http://www.minsocam.org/

deposits (Hua et al. 2003; Hu et al. 2017; Jiang et al. 2020).

Southern Hunan Province is located in the western portion of the Nanling metallogenic belt of South China, which is a world-class tungsten-tin mineral district. This province consists of several W-Sn-Pb-Zn-Cu polymetallic deposits, including the Dengfuxian, Dayishan, Shizhuyuan, Xianghualing, and Jiuyishan deposits (Fig. 1c; Li et al. 2018b; Wu et al. 2018, 2021; Yuan et al. 2018; Jiang et al. 2020; Liao et al. 2021; Zhu et al. 2021), most of which are distributed along major NW-SE- and NE-SW-trending faults (Li and Sasaki 2007). Magmatic rocks in this area were emplaced during three discrete stages, i.e., the Early Paleozoic (542-360 Ma), the Triassic (251-200 Ma), and the Jurassic (195-146 Ma; Hu et al. 2017). Of these magmatic episodes, the Jurassic granites are the most closely associated with W-Sn-Pb-Zn-Cu polymetallic deposits and, hence, have attracted considerable scientific and commercial interest (Mao et al. 2007; Hu et al. 2017; Yan et al. 2018).

DEPOSIT GEOLOGY

Southern Hunan Province contains several Sn-polymetallic deposits located in proximity to the Chenzhou-Linwu Fault (Fig. 1c). These bodies are often spatially associated with highly differentiated granites.

Dengfuxian deposit

The Dengfuxian (DFX) deposit, located in Chaling County, is a W-Sn-Nb-Ta-Pb-Zn polymetallic deposit hosted by the Dengfuxian Granite Complex. The ore occurs in a series of quartz veins that are controlled by a network of closely spaced NEE-oriented fractures. The main ore minerals include cassiterite, wolframite, molybdenite, arsenopyrite, pyrite, chalcopyrite, pyrrhotite, galena, sphalerite, scheelite, and quartz with minor fluorite, sericite, and chlorite constituting the gangue minerals (Xiong et al. 2020). The major wallrock alterations that accompanied formation of these ore minerals include muscovitization, silicification, sericitization, chloritization, and dolomitization.

The Dengfuxian Pluton is a large granitic complex that is spatially and genetically associated with a Sn polymetallic deposit (Xiong et al. 2019, 2020). The granitic rocks in this composite pluton cover a total area of about 171 km^2 and were emplaced in three main stages (Fig. 2a). Stage I is represented by coarse-grained and porphyritic biotite granites emplaced at ca. 230.0 ± 1.6 Ma (Huang et al. 2011). Stage II was marked by emplacement of a medium- to fine-grained two-mica granite at 154.0 ± 2.2 Ma (Huang et al. 2013), and its associated mineralization has yielded a molybdenite Re-Os isochron age of 150.5 ± 5.2 Ma (Cai et al. 2012). Stage III is represented by a fine-grained muscovite granite emplaced at 145.2 ± 0.9 Ma (Xiong et al. 2020). Sedimentary and metamorphic rocks spatially associated with the Dengfuxian polymetallic deposit include limestone of the Lower Permian Longtan Formation as well as metamorphosed sandstone, slate, and phyllite of middle Cambrian age (Xiong et al. 2020).

Dayishan deposit

The Dayishan (DYS) deposit is located about 30 km northwest of Chenzhou city in southern Hunan Province. This Sn deposit is spatially related to the Dayishan Granitic Complex, which can be divided into four units, from oldest to youngest: the Shuangfengan Unit (Triassic), Guankou Unit (Early Jurassic), Tangshipu Unit (Middle Jurassic), and Nibatian Unit (Late Jurassic) (Sun et al. 2018, 2021; Zhang et al. 2021). Granite related to tin mineralization was emplaced mainly in the Jurassic (Sun et al. 2018). The granites of the Dayishan Granitic Complex were intruded into carbonate strata of the Devonian to Carboniferous age, which overlie shale, conglomerate, and sandstone beds of the Ordovician age. Major structures in the area include NW-trending faults and NNE-trending anticlinal folds (Fig. 2b).

Well-studied ore bodies in the study area include the Tengshan'ao and Maozaishan deposits. The mineralization is associated with greisen-quartz veins and altered granites, both of which are associated with potash alteration, silicification, and greisenization (Sun et al. 2018, 2021; Zhang et al. 2021). Cassiterite, the major ore mineral in this deposit, is closely associated with arsenopyrite, chalcopyrite, pyrite, sphalerite, and molybdenite. Common gangue minerals are quartz, potassium feldspar, tourmaline, muscovite, topaz, albite, sericite, and chlorite (Sun et al. 2018, Zhang et al. 2021).

Shizhuyuan deposit

The Shizhuyuan (SZY) deposit is a multistage W-Sn-Mo-Bi deposit located 16 km southeast of Chenzhou city. This deposit is closely associated with the Qianlishan Granite Complex, which covers a total area of ~11 km^2 and consists of three intrusive stages: Stage I is a microfine-grained porphyritic biotite granite with an emplacement age of 183.2-152.3 Ma (Liu et al. 1997; Chen et al. 2016; Liao et al. 2021); Stage II is a fine-grained biotite granite with an intrusion age of 162.6-137.4 Ma (Liu et al. 1997; Yin et al. 2002; Li et al. 2004; Chen et al. 2016; Liao et al. 2021); and Stage III is a medium-grained equigranular zinnwaldite granite and granite porphyry, intruded at 154.4-144.4 Ma (Liu et al. 1997; Chen et al. 2016; Liao et al. 2021). Other units in the area include Sinian metasedimentary rocks, Devonian carbonate, and clastic sedimentary rocks. The Devonian rocks are the most significant ore-bearing host rocks and can be subdivided into four formations (from bottom to top): (1) Tiaomajian Formation, (2) Qiziqiao Formation, (3) Shetianqiao Formation, and (4) Xikuangshan Formation.

This is the peer-reviewed, final accepted version for American Mineralogist, published by the Mineralogical Society of America.
The published version is subject to change. Cite as Authors (Year) Title. American Mineralogist, in press.
DOI: https://doi.org/10.2138/am-2022-8823. http://www.minsocam.org/

The W-Sn-Mo-Bi mineralization is structurally controlled by NE-trending faults and fractures (Fig. 2c). The styles of mineralization include greisen-quartz vein Sn-Cu ore, disseminated W-Sn-Mo-Bi ore in skarn, greisen-skarn-type W-Sn-Mo-Bi ore, and disseminated W-Sn-Mo-Bi-type ore in greisen at the roof of the porphyritic biotite granite pluton (Liao et al. 2021). The major ore minerals are cassiterite, wolframite, scheelite, molybdenite, bismuthinite, arsenopyrite, pyrrhotite, pyrite, magnetite, sphalerite, galena, and chalcopyrite. The common gangue minerals are potassium feldspar, albite, quartz, muscovite, topaz, and fluorite (Liao et al. 2021). The major hydrothermal alterations that accompanied ore formation are skarn metasomatism, tourmalinization, and greisenization.

Xianghualing deposit

The Xianghualing (XHL) deposit is located in northern Linwu County, Hunan Province, proximally to the Laiziling plutons. The Laiziling Pluton covers a total area of 2.2 km^2 and has yielded a zircon U-Pb age of 156.4 ± 1.4 Ma (Yang et al. 2018). It can be divided into four vertical zones, from top to bottom, the pegmatite, greisen, albite granite, and albite microcline granite zones (Wu et al. 2018). Minor rocks in this area include shallow-marine sand and clay deposits of Cambrian age, shallow-marine carbonates of Devonian to Carboniferous age, and sandstones and shales ranging from the Permian to Cretaceous in age. NE-trending faults and fractures are the main ore-bearing structures (Fig. 2d).

The style of mineralization is skarn type, and hydrothermal alteration processes such as chloritization accompanied the formation of major ore minerals including cassiterite, pyrrhotite, pyrite, arsenopyrite, sphalerite, magnetite, and galena. Common gangue minerals in the deposit are actinolite, tremolite, diopside, garnet, and wollastonite (Wu et al. 2018).

This is the peer-reviewed, final accepted version for American Mineralogist, published by the Mineralogical Society of America.
The published version is subject to change. Cite as Authors (Year) Title. American Mineralogist, in press.
DOI: https://doi.org/10.2138/am-2022-8823. http://www.minsocam.org/

Jiuyishan deposit

The Jiuyishan (JYS) deposit, located in southwestern Hunan Province, is one of the most important W-Sn deposits in the Nanling region of China. This deposit is closely related to the Jiuyishan Granitic Complex, which consists of the Xuehuading, Pangxiemu, and Jinjiling plutons, covering 130 km^2, 350 km^2, and 49 km^2, respectively (Fig. 2e; Su 2017). Although the Xuehuading Pluton dates to the Early Paleozoic (432.0 ± 21.0 Ma; Fu et al. 2004), the other granites were emplaced in the Jurassic (156-145 Ma), with cross-cutting relationships demonstrating Pangxiemu to be younger than Jinjiling (Liu et al. 2019; Li et al. 2021). This area, which also exposes carbonates of Devonian to Triassic age, is dominated by NNE- and N-trending fractures, accompanied by NE-, NW-, and E-trending faults.

The main W-Sn deposits in the Jiuyishan area, e.g., Da'ao, Shazichong, and Xiangyuan, are concentrated in the western part of the Jinjiling Pluton and exhibit diverse mineralization types including disseminated greisen-type, altered granite-type, and greisen-quartz vein-type (Fu et al. 2007). Greisenization and silicification were the major hydrothermal alteration processes that accompanied formation of the main ore minerals, which include cassiterite, wolframite, pyrite, chalcopyrite, sphalerite, and molybdenite. Common gangue minerals are potassium feldspar, plagioclase, topaz, albite, quartz, and muscovite (Fu et al. 2007).

SAMPLING AND ANALYTICAL METHODS

Representative samples of Sn ore were collected from the five deposits. Sample DFX is from a sulfide-bearing W-Sn quartz vein in muscovite granite of the No. 13 tunnel of the Dengfuxian tungsten deposit (Fig. 3a-c), and sample DYS is from the greisen ore body (ore vein width 1 m) of the Xilingxi granite in Dayishan (Fig. 3d-f). Sample SZY is from the greisen-skarn vein (not intensely skarn mineralized) of the

This is the peer-reviewed, final accepted version for American Mineralogist, published by the Mineralogical Society of America.
The published version is subject to change. Cite as Authors (Year) Title. American Mineralogist, in press.
DOI: https://doi.org/10.2138/am-2022-8823. http://www.minsocam.org/

No. 490 tunnel of the Shizhuyuan deposit (Fig. 3g-i), sample XHL is from the skarn-related Sn- and As-bearing granite in exploration line No. 47 of Tunnel 272 of the Xinfeng Ore Block (Fig. 3j-l), and sample JYS is from the greisen-quartz vein of the Xiangyuan mine (Fig. 3m-o).

After observation by optical microscopy (Fig. 4), each sample was crushed and different phases were separated for further analysis. The analytical techniques used in this study, i.e., cathodoluminescence (CL) imaging and mapping, geochronology and trace elements analyses, and statistical methods (PCA and OPSL-DA) are detailed in the Supplementary Material 1 (10.6084/m9.figshare.22187755) and have been made publicly available in Figshare (https://figshare.com/account/home, 2023/02). SnO_2 reserve data for the tin deposits involved in this study were obtained from the National Geological Archive of China (https://www.ngac.cn/, 2023/02).

RESULTS

Cassiterite petrography

All five of the studied tin deposits contain only a single generation of cassiterite, each showing similar textural characteristics. Sample DFX grains are quasi-automorphic, grayish-yellowish in color, ~400 μm in diameter, and lightly altered (Fig. 4a-b). Sample DYS grains are yellow-brown, up to 1 mm in diameter (the largest among the five deposits), and strongly altered in greisen veins (Fig. 4c-d). Sample SZY grains are irregular in shape, yellow-brown, ~200 μm in size, and strongly altered (Fig. 4e-f). Sample XHL grains are elongated (~300 μm in length) and usually broken, gray-yellow (Fig. 4g-h). Sample JYS grains are quasi-automorphic, brown, and ~200 μm in size, and strongly altered (Fig. 4i-j).

Cassiterite U-Pb geochronology

Analytical results of cassiterite U-Pb dating are presented in Supplementary Material 2 (10.6084/m9.figshare.22187752). Analyzed grains range in size from 70 to 300 μm and in color from dark grey to black, most having euhedral to subhedral shapes and displaying evident oscillatory zonation or patchiness in CL images (Fig. 5a-e). They frequently contain hydrothermal alteration veins or veinlet cracks. These characteristics can provide a reference for the location of laser ablation spots, and avoid the ablation of grains with exceptionally low or high U or Pb contents (which are usually pure black or off-white) prone to yielding poor intercept ages. Because the 128 cassiterites tested have relatively low U (0.1-53 ppm) and Th (0-6.5 ppm) contents, crystallization ages and initial $^{207}Pb/^{206}Pb$ are calculated from a Tera-Wasserburg concordia plot. Cassiterite analyses from the five deposits form Tera-Wasserburg isochrons defining lower-intercept dates of 142.0 ± 17.1 Ma (MSWD = 1.40; n = 25, initial $^{207}Pb/^{206}Pb$ = 0.884 ± 0.020) for Dengfuxian (Fig. 6a), 154.7 ± 3.0 Ma (MSWD = 0.96; n = 40, $^{207}Pb/^{206}Pb$ = 0.852 ± 0.013) for Dayishan (Fig. 6b), 154.9 ± 2.1 Ma (MSWD = 1.50; n = 21, $^{207}Pb/^{206}Pb$ = 0.851 ± 0.081) for Shizhuyuan (Fig. 6c), 155.4 ± 4.8 Ma (MSWD = 0.43; n = 20, $^{207}Pb/^{206}Pb$= 0.833 ± 0.018) for Xianghualing (Fig. 6d), and 152.0 ± 5.8 Ma (MSWD = 1.50; n = 23, $^{207}Pb/^{206}Pb$ = 0.828 ± 0.007) for Jiuyishan (Fig. 6e). Overall, cassiterites from the five deposits yielded lower intercept ages that range from 155.4 ± 4.8 Ma to 142.0 ± 17.1 Ma, indicating a Late Jurassic to earliest Cretaceous age of formation.

Trace element compositions

The trace element compositions of cassiterite grains from the five studied W-Sn deposits are given in Supplementary Material 2 (10.6084/m9.figshare.22187752). To show more clearly the trace element characteristics of cassiterite in each type of deposit, we present here a pooled dataset (note: all ranges represent 16^{th}-84^{th} percentiles in order to avoid the influence of outliers).

Cassiterite in the quartz vein-type deposit (DFX) has the highest concentrations of Fe (median = 1892 ppm, 243-5091 ppm), Mn (median = 8.5 ppm, 1.1-171 ppm) and W (median = 4224 ppm, 51.6-18799 ppm), and the lowest concentrations of Zr (median = 8.3 ppm, 3.8-14.0 ppm), U (median = 0.8 ppm, 0.3-1.3 ppm), Nb (median = 20.3 ppm, 7.3-278 ppm), Ta (median = 2.2 ppm, 0.2-4.4 ppm) and Hf (median = 0.5 ppm, 0.1-1.2 ppm).

Cassiterite in the greisen-skarn-type (SZY) deposit has the highest concentrations of Ti (median = 1067 ppm, 352-4701 ppm) and U (median = 34.1 ppm, 25.8-47.3 ppm), but rather low concentrations of Nb (median = 302 ppm, 163-549 ppm), Ta (median = 83.0 ppm, 44.9-122 ppm), Zr (median = 203 ppm, 127-347 ppm) and Hf (median = 15.9 ppm, 6.2-26.4 ppm).

Cassiterites in both the granite-type (XHL) and greisen-type deposits (DYS and JYS) contain relatively high concentrations of Nb (XHL, median = 567 ppm, 101-1367 ppm; DYS, median = 2772 ppm, 1582-5513 ppm; JYS, median = 1867 ppm, 315-9789 ppm), Ta (XHL, median = 680 ppm, 92-1763 ppm; DYS, median = 292 ppm, 189-1019 ppm; JYS, median = 994 ppm, 15.5-3788 ppm), Zr (XHL, median = 145 ppm, 57.2-145 ppm; DYS, median = 151 ppm, 101-283 ppm; JYS, median = 118 ppm, 37.1-498 ppm), Hf (XHL, median = 43.0 ppm, 13.9-48.4 ppm; DYS, median = 19.8 ppm, 12.7-45.5 ppm; JYS, median = 10.0 ppm, 2.1-74.4 ppm), and Ti (XHL, median = 2023 ppm, 742-2576 ppm; DYS, median = 97.0 ppm, 47.3-163 ppm; JYS, median = 1139 ppm, 376-1675 ppm). The total REE (ΣREE) contents of cassiterites from all five deposits are quite low and not significantly different (DFX, 0-0.40 ppm; DYS, 0-0.40 ppm; SZY, 0-1.00 ppm; XHL, 0-0.40 ppm; JYS, 0-0.43 ppm), and REEs

DOI: https://doi.org/10.2138/am-2022-8823. http://www.minsocam.org/

of importance (i.e., Eu and Ce) will be considered in the Discussion section below.

DISCUSSION

Timing of the Sn-polymetallic mineralization

Only small amounts of U and Th usually partition into cassiterite, which precludes considerable radiation-related damage of the mineral (Lehmann et al. 2021). Thus, in situ U-Pb dating of cassiterite provides a robust constraint on the timing of evolved magmatic or magmatic-hydrothermal systems responsible for rare-metal mineralization (Zhang et al. 2017). In this section, we discuss our newly obtained cassiterite U-Pb crystallization ages in the context of the magmatic and metallogenic evolution of the five studied deposits of southern Hunan Province (Fig. 7). Overall, these ages offer novel insights into the timing of magmatic-hydrothermal processes responsible for the production of the largest Sn reserves in China.

The main episode of tin mineralization at Dengfuxian is considered to be associated with the formation of Stage II granites (Cai et al. 2012; Huang et al. 2013). However, recent studies have found that the muscovite granite (i.e., Stage III granite), which was the product of residual magma fractional crystallization, also has tin mineralization potential (141-137 Ma; Xiong et al. 2020). Our cassiterite grains are spatially correlated with the Stage III granite, and the U-Pb dating results (142.0 ± 17.1 Ma) also support this relationship despite significant age uncertainty. The main reason for the large age uncertainty is the very low U and Pb contents of these cassiterite grains, which were probably precipitated late in the mineralization history of the deposit. This observation implies that Early Cretaceous granites (~145-130 Ma) in this region have a strong potential for Sn-polymetallic mineralization.

There is as yet no consensus on the emplacement age of the numerous granite bodies in the Dayishan area (Zeng 2013). Geochronological studies of granite-associated deposits can help to resolve this issue. Several radiometric studies have yielded Middle Jurassic dates, e.g., 151.1 ± 1.5 Ma for a muscovite ^{40}Ar-^{39}Ar plateau age of the Tengshan'ao deposit (Zhang et al. 2021), 157.9 ± 7.7 Ma for a molybdenite Re-Os isochron age of the Maozaishan deposit (Sun et al. 2018), and 156.5 ± 2.8 Ma for a cassiterite U-Pb age of the Maozaishan deposit (Sun et al. 2018). The geochronological results for these nearby deposits overlap, within analytical uncertainty, with our cassiterite U-Pb date of 154.7± 3.0 Ma, thus suggesting that tin mineralization in the Dayishan area was related to the intrusion of granite plutons and occurred during the Late Jurassic.

Cassiterite grains from the Shizhuyuan deposit yield a concordia intercept age of 154.9 ± 2.1 Ma, which is more precise than existing zircon U-Pb ages of ca. 160-150 Ma reported for the porphyritic biotite granite hosting this deposit (Chen et al. 2016). This date overlaps with a molybdenite Re-Os isochron age of 151.0 ± 3.5 Ma reported for W-Sn-Mo-Bi mineralization (Li and Mao 1996), which also supports late-stage formation of greisen-skarn-type cassiterite in the SZY deposit, during which granitic fluids provided the heat source and metals (Liao et al. 2021).

The age of Sn mineralization of the Xianghualing deposit is constrained by in situ U-Pb dating of cassiterite, which yielded a Tera-Wasserburg lower intercept age of 155.4 ± 4.8 Ma (MSWD = 0.43), consistent with a zircon U-Pb age of 156.4 ± 1.4 Ma reported for granite of the Laiziling Pluton (Yang et al. 2018). This finding suggests that Sn mineralization was coeval with granite emplacement.

Finally, our U-Pb cassiterite date for the Jiuyishan deposit (152.0 ± 5.8 Ma) agrees, within analytical uncertainty, with the Re-Os molybdenite date of the greisen-quartz vein of the Da' ao tin mine (151.3 ± 2.4 Ma, Fu et al. 2007) and the

U-Pb age of zircons from the Jinjiiling granite with which it is spatially associated (156.4 ± 0.7 Ma, Li et al. 2021).

Overall, cassiterite grains from the five studied tin deposits yield a relatively narrow range of Late Jurassic to earliest Cretaceous ages (155.4 to 142.0 Ma), indicating that the deposits are temporally linked to the multistage emplacement of granitic plutons in the study area (Xiong et al. 2020). In a geodynamic context, the Middle Jurassic to Early Cretaceous (180-125 Ma) magmatism and tin-tungsten mineralization events in the South Ridge area may have been related to the westward subduction of Pacific Ocean lithosphere beneath the Eurasian continent, which triggered asthenospheric upwelling owing to lithospheric thinning in an extensional tectonic setting (Mao et al. 2007). The new cassiterite U-Pb ages determined here overlap with the main mineralization interval (165-150 Ma) of the world-class W-Sn metallogenic province in the Nanling region (Mao et al. 2007). However, the timescale of W-Sn mineralization in southern Hunan Province extends into the earliest Cretaceous, possibly due to the continued enrichment of mineralizing elements in residual magmas (Xiong et al. 2019, 2020). This inference indicates that Early Cretaceous granites in the study area should be regarded as targets for W-Sn exploration.

Cassiterite compositions trace the nature of ore-forming fluids

Origin of Sn. Cassiterite typically contains a wide range of trace elements such as Ti, Nb, Ta, Fe, Mn, and W, which can either substitute for Sn^{4+} in the mineral lattice or be present in the form of exsolved mineral inclusions (Taylor 1979). These trace elements can be used to track the nature of mineralizing fluids as well as the growth environment of the mineral (Tindle and Breaks 1998; Cheng et al. 2019; Wu et al. 2021). In particular, Nb, Ta, Fe, W, and Mn in cassiterite are often used to determine the type of tin deposits and the origin of tin-bearing fluids (Tindle and Breaks 1998). A Nb+Ta versus Fe+Mn discriminant diagram shows that all five deposits are typical magmatic-hydrothermal tin deposits related to granite (Fig. 8). Considering the possible positive correlation between iron and tungsten content in cassiterite (Yu and Jiang 2001) and that sample DFX is a quartz vein-type sample dominated by W in a W-Sn deposit (n.b. the only one out of the five studied deposits), the contents of W and Fe in this sample are high (Fig. 9d). Moreover, its low Nb and Ta contents are consistent with its origin as a hydrothermal vein-type cassiterite (Möller et al. 1988; Fig. 9a).

Metallogenesis temperature. Previous studies of tin deposits have shown that the concentrations of HFSEs such as Nb, Ta, Zr, and Hf in cassiterite reflect the temperature of the mineralizing fluid. Specifically, cassiterite formed at high temperatures is more enriched in Nb, Ta, Zr, and Hf than that formed at low temperatures (Cheng et al. 2019; Gemmrich et al. 2021; Hu et al. 2021; Wu et al. 2021). In addition to temperature, the early-precipitated minerals play a crucial role in controlling the chemical composition of later-formed minerals. Experimental studies of the partitioning of HFSEs in zircons have shown that Hf in the residual melt or hot liquid decreases substantially at lower temperatures (Wang et al. 2010). Furthermore, because HFSE-enriched accessory minerals are more enriched in Ta relative to Nb in felsic melts (D_{Nb}/D_{Ta} = 0.3-0.4 for sphene, 0.6-0.7 for rutile, 0.7-0.8 for ilmenite, and 0.8 for titanomagnetite in high-silica rhyolites; Green and Pearson, 1987), their precipitation leads to greater enrichment of Nb relative to Ta and Zr relative to Hf in the residual melt and associated fluid phase. Therefore, variation in the elemental composition of cassiterite is a function of temperature and mineral fractionation (Wu et al. 2021). During high-temperature mineralization events (e.g., greisen and granite),

DOI: https://doi.org/10.2138/am-2022-8823. http://www.minsocam.org/

hydrothermal fluids become enriched in Nb, Ta, Zr, and Hf, which can then be readily incorporated into the cassiterite lattice by isomorphic substitution. As the temperature of the ore-forming fluid decreases, cassiterites precipitated at this stage (e.g., skarn and veins) show a sharp decrease in HFSEs, and the Zr/Hf and Nb/Ta ratios increase with the precipitation of incompatible element-enriched minerals (Fig. 9a-c). The high contents of Nb, Ta, Zr, and Hf in cassiterite grains from greisen, greisen-quartz veins, and altered granites (e.g., samples DYS, JYS, and XHL) indicate that they were formed from higher-temperature fluids than cassiterite grains from greisen-skarn and quartz veins (e.g., samples SZY and DFX), which have lower Nb, Ta, Zr, and Hf contents (Fig. 9a-c). Thus, Nb, Ta, Zr, and Hf contents are indicative of mineralization temperatures (Fig. 9a-c), which is consistent with the results of other geothermometers that have been applied to these deposits (Xiong et al. 2019; Wang et al. 2020; Zhao et al. 2022a, b).

Variable chemistry of ore-forming fluids. Differences in chemical composition and physio-chemical conditions between ore-forming fluids of tin mineralization and the precursor magma are reflected in the HFSE content of cassiterite, its precipitation temperature, and the type of tin mineralization (Cheng et al. 2019; Wu et al. 2021). In a geochemical system that is characterized by charge- and radius-controlled (ChaRaC) behavior, some trace-element pairs with similar ionic radii and valence states (e.g., Nb-Ta and Zr-Hf) exhibit coherent behavior and maintain chondritic to near-chondritic ratios (Bau 1996; Rudnick et al. 1993). Moreover, the interelement ratios measured in magmatic systems can be influenced by chemical reactions and fluid mixing, and non-ChaRaC behavior reflects a specific magmatic-hydrothermal system that is highly evolved and enriched in H_2O, Li, B, F, P, and/or Cl (Bau 1996). Cassiterites from the five studied W-Sn deposits have a wide range of Nb/Ta ratios

DOI: https://doi.org/10.2138/am-2022-8823. http://www.minsocam.org/

(DFX 14.16-68.5; DYS 6.64-15.4; XHL 3.79-45.0; SZY 5.43-54.0; JYS 7.36-48.0) and Zr/Hf ratios (DFX 1.04-297; DYS 0.85-14.8; XHL 0.33-81.6; SZY 0.52-14.6; JYS 0.81-718), implying derivation from a highly evolved melt. The wide range of Nb/Ta and Zr/Hf ratios of cassiterite in these deposits (Fig. 9a-c) can be explained by the influence of multiple processes, as described in previous studies. For example, quartz vein-type cassiterite (DFX) can be produced by fluid immiscibility (Xiong et al. 2019), greisen-skarn-type cassiterite (SZY) by mixing ore-forming magmatic fluid with meteoric water (Zhu et al. 2015), and greisen-type cassiterite (DYS and JYS) by fluid-rock interactions (Korges et al. 2018; Schmidt et al. 2020; Liu et al. 2021; Zhao et al. 2022a, b). In Nb-Ta-Zr-Hf discriminant plots (Fig. 9a-c), granite-type cassiterite (XHL) exhibits a limited range of Nb/Ta and Zr/Hf ratios. In contrast, the greisen-type cassiterite is more enriched in magmatic volatiles such as F and B, with the hydrothermal fluid source of DYS exhibiting a narrower range of Nb/Ta and Zr/Hf ratios than that of JYS (Rubin et al. 1993; Cheng et al. 2019; Zhao et al. 2022a, b).

Titanium (Ti) and uranium (U) are both incompatible elements that are difficult to incorporate into the mineral lattice of rock formations, and they tend to be relatively enriched in residual magmas and hydrothermal fluids (Han et al. 2003). The Ti and U concentrations in cassiterite are thought to be related to the degree of evolution of the parent magma, but the mechanism of their uptake during mineral precipitation is not well understood (Hu et al. 2021). To gain a deeper understanding of the influence of associated granites on the Ti and U contents of cassiterite, we conducted a comparative Ti-U analysis of the cassiterite and associated granites in the five studied tin deposits. Interestingly, our findings suggest that the Ti and U contents of cassiterite are positively influenced by their associated granites (Fig. 10). Although both are incompatible elements, Ti is relatively less incompatible than U and more

DOI: https://doi.org/10.2138/am-2022-8823. http://www.minsocam.org/

easily enters the cassiterite lattice. Additionally, the ionic radius of Ti (0.605Å) is slightly smaller than that of Sn (0.69Å), allowing it to readily replace Sn in cassiterite (Cheng et al., 2019), leading to lower TiO_2 contents in highly evolved tin-bearing granites. Combined with the fact that sample XHL is associated with evolved granites, this may be the reason for the low Ti content of the DYS sample, whereas the Ti content of cassiterite in the low-TiO_2 Laiziling granite is not low (Fig. 10a). Furthermore, the consistent geochemical behavior of the cassiterite and associated granites of these deposits in terms of U content confirms that the granite associated with quartz vein-type tin ore exhibits the lowest degree of evolution among the associated granites (Fig. 10b). In summary, Ti and U concentrations reflect the degree of evolution of granitic parent magmas for tin mineralization, with an increasing evolutionary degree from quartz vein-type to greisen-type to granitic-type cassiterite.

Redox conditions of ore-forming processes. Patterns of REE distribution in cassiterite have been used to constrain the source(s) of ore-forming fluids, the physicochemical characteristics of the fluids, and the dynamics of hydrothermal systems (Brugger et al. 2000; Wu et al. 2021). Four of the five of the studied deposits (excepting XHL) contain minerals coprecipitated with cassiterite that can affect the REE patterns of the latter, i.e., wolframite and/or scheelite at DFX, SZY, and JYS, and tourmaline at DYS. For this reason, the following discussion will focus on the REE behavior of cassiterite, wolframite, scheelite, tourmaline, and hydrothermal fluids.

The direction (i.e., positive or negative) and size of the Eu anomaly in hydrothermal minerals are chiefly controlled by three factors: (1) the redox state of the fluid, (2) the partitioning coefficients of Eu^{2+} and Eu^{3+} between the host mineral and the fluid, and (3) the Eu content of the fluid (Shannon 1976). In oxidizing systems, given the significantly smaller ionic radius of Sn^{4+} (0.69 Å) relative to Eu^{2+} (1.25 Å)

This is the peer-reviewed, final accepted version for American Mineralogist, published by the Mineralogical Society of America.
The published version is subject to change. Cite as Authors (Year) Title. American Mineralogist, in press.
DOI: https://doi.org/10.2138/am-2022-8823. http://www.minsocam.org/

and Eu^{3+} (1.07 Å), valence changes have a limited effect on the Eu anomaly of cassiterite. In this case, cassiterite directly inherits the Eu anomaly of the ore-forming fluid because of the similar geochemical behavior of Eu^{3+} to other REEs (Wu et al. 2021). On the contrary, when the ore-forming fluid is reducing, Eu^{2+} readily replaces Ca^{2+} (1.12 Å) because of their equivalent electrovalences and similar ionic radii. In addition, Eu^{2+} tends to partition more readily into wolframite, scheelite and tourmaline in a reducing environment (Sverjensky 1984; Brugger et al. 2000; Zhu et al. 2014), resulting in a negative Eu anomaly in cassiterite. In this study, samples DFX, DYS, SZY, and JYS show significant negative Eu anomalies (Fig. 11), reflecting the reducing condition of the ore-forming fluids, whereas sample XHL from the Laiziling Granite has no Eu anomaly, indicating that its crystallization environment was probably less reducing than those of the other four deposits.

Little is known about the factors controlling the Ce content of cassiterite. Precipitation of cassiterite and scheelite does not require high-fO_2 conditions (Schmidt, 2018). The geochemical behavior of Ce^{3+} under reducing conditions is similar to that of other REEs, and the Ce anomalies in hydrothermal minerals may reflect the REE patterns of their precipitation environments unless Ce-rich minerals (e.g., monazite) are coprecipitated. Conversely, in an oxidizing magmatic-hydrothermal system, Ce^{4+} (0.97 Å) becomes more incompatible than Ce^{3+} (1.14 Å) due to the larger difference in its ionic radius from Ca^{2+} (1.12 Å), resulting in negative Ce anomalies in cassiterite, wolframite, and scheelite following precipitation of Ce-rich minerals like monazite (Wu et al. 2021). Based on the lack of significant Ce anomalies in cassiterite (Fig. 11), we infer that tin mineralization in southern Hunan Province occurred in a reducing environment.

To summarize, the characteristic behavior of trace elements in cassiterite indicates that the crystallization of that changes in physicochemical conditions (e.g., temperature) during highly evolved magmatic hydrothermal processes are important factors driving the precipitation of Sn-enriched minerals, but the redox conditions of the precipitated liquid are irrelevant. Based on our findings, we suggest that progressively more evolved granites are responsible for quartz vein-type, greisen-type, and granite-type cassiterite respectively. Through this magmatic sequence, the HFSE contents of cassiterite gradually increased and their ranges of variation gradually decreased, implying a relationship between these two patterns that need further study.

Substitution mechanism of trace elements in cassiterite

We evaluated the trace element assemblages of cassiterite in the five studied tin deposits using two chemometric methods (PCA and OPLS-DA). The PCA results reveal coupling between trace elements in cassiterite, with the first two components accounting for 62.0% of total variance (36.4% for PC1, and 25.6% for PC2), demonstrating the feasibility of dimensionality reduction. The main elemental loadings are Nb, Ta, Zr, and Hf on PC1, and Fe, Mn, and W on PC2 (Fig. 12). In Figure 12, vector angles smaller than 90° indicate a positive correlation between elemental pairs, as for Fe + Mn vs. Nb + Ta (r = +35.20°; Fig. 8a), W vs. Fe (r = +67.54°; Fig. 9d), and Nb + Ta vs. Fe (r = +22.56°; Fig. 9f). Therefore, the typical trace element substitution mechanisms of $(Fe, Mn)^{2+} + 2(Nb, Ta)^{5+} = 3Sn^{4+}$, $W^{6+} + 2Fe^{3+} = 3Sn^{4+}$, and $Fe^{3+} + (Nb, Ta)^{5+} = 2Sn^{4+}$ (Černý and Ercit 1985; Černý et al. 1985; Cohen et al. 1985; Möller et al. 1988) can be confirmed in the cassiterite samples of DYS, SZY, XHL, and JYS. However, the mechanism of trace element substitution in the lattice of cassiterite from the tungsten-dominated quartz vein-type cassiterite is dominantly $W^{6+} + 2Fe^{3+} = 3Sn^{4+}$.

The PCA plot reveals the general similarities of the trace element assemblages in the cassiterite of all five tin deposits. To better investigate differences in their trace element assemblages, we made use of OPLS-DA. In plots of this type, R^2X_{cum} shows differences in variables between groups, and R^2Y_{cum} indicates differences in variables within groups. The five studied tin deposits exhibit large differences in the trace element assemblages of cassiterite (for each deposit, $R^2X_{cum} > 0.5$; Fig. 13). This observation indicates that the nature and content of trace elements in cassiterite are significantly different depending on mineralization type and location.

Insights for W-Sn exploration

The in situ cassiterite U-Pb ages of the present study offer insights regarding genetic links between Sn-polymetallic ores and their spatially related granites in southern Hunan Province, with useful implications for exploration of economically significant deposits. Critical elements (W, Sn, Cu, Pb, Zn) in granites of the Nanling region show a gradual increase from Early Paleozoic (542-360 Ma) to Triassic (251-200 Ma), Jurassic (195-146 Ma), and Cretaceous (145-80 Ma) plutons, with tungsten and tin being especially enriched in Early Cretaceous granites (Liu et al. 2022b). This trend conforms broadly to the size of mining operations in southern Hunan Province, with Early Paleozoic deposits being non-productive, Triassic deposits being rather small (e.g., Longshang deposit, 16 Kt SnO_2; Liu et al. 2022), and Jurassic deposits being quite large (e.g., Hehuaping, 130 Kt SnO_2; Yao et al. 2014). However, the comparatively small size of mines extracting Cretaceous-age ores (e.g., the Jiepailing deposit, 92.1±0.7 Ma, 48 Kt SnO_2; Yuan et al. 2015) is not commensurate with their high concentrations of mineralized elements (W, Sn, Cu, Pb, Zn), and Early Cretaceous plutons warrant closer inspection in the future as possible mining targets.

Based on previous studies of the southern Hunan tin province and the present study of its geochronology, the magmatic emplacement and metallogenic evolution of this province can be summarized as occurring in three main stages (Li et al. 2018a; Luo et al. 2022; Liu et al. 2022b): (1) Stage I (Early Paleozoic and Triassic), during which magma was formed by melting of lower crust and enrichment of tungsten and tin occurred through crustal-mantle interactions; (2) Stage II (Jurassic), during which magma was emplaced at high crustal structural levels where it reacted with wall rocks and extracted metals to further enrich tin-tungsten ores; and (3) Stage III (Cretaceous), during which magmatic-hydrothermal reactions were superimposed on earlier mineralization events. Small dykes and deeper intrusions formed during the Early Cretaceous, with associated hydrothermal fluids depositing additional tin and tungsten (Fig. 14a). Therefore, ore exploration should focus on the highly evolved granites from the late stages of granite complex formation.

Previous and present studies have inferred that the contents of Nb, Ta, Zr, and Hf and the ratios of Nb/Ta and Zr/Hf gradually decrease from granite-type to greisen-type and then to quartz vein-type cassiterites (Cheng et al. 2019; Hu et al. 2021; Wu et al. 2021). However, previous studies have not used the chemical behavior of these trace elements to analyze the distance between deposits and magmatic systems associated with intrusive rocks. In a systematic study of tin deposits in the Bolivian tin metallogenic belt, Gemmrich et al. (2021) concluded that variations in trace element content of ores emplaced at different levels within the xenothermal and epithermal environments recorded genetic compositional trends. Deposits that formed proximally to related intrusive complexes are typically enriched in Nb and Ta relative to epithermal and shallow xenothermal deposits. The present study shows that similar patterns of enrichment of Nb, Ta, and other HFSEs are present in the tin deposits of southern Hunan Province, which are more closely

DOI: https://doi.org/10.2138/am-2022-8823. http://www.minsocam.org/

associated with granitic bodies than other types of tin mineralization (Sun et al. 2018; Zhang et al. 2021; Zhao et al. 2022a, b). The sum of these elements provides a solid ground for the establishment of a comprehensive, idealized tin metallogenic model for the southern Hunan tin province and similar provinces worldwide (Fig. 14b).

IMPLICATIONS

A combination of cassiterite cathodoluminescence, U-Pb geochronology, and trace-element data offers important insights into the nature of ore-forming fluids and the extended formation history of Sn-polymetallic deposits in the southern Hunan tin province, as follows:

1. LA-ICP-MS in situ cassiterite U-Pb dating of five major deposits (i.e., Dengfuxian, Dayishan, Shizhuyuan, Xianghualing, and Jiuyishan) yielded ages ranging from 155.4 to 142.0 Ma, corresponding to the Late Jurassic to earliest Cretaceous. These ages indicate that these deposits are temporally and genetically linked to their spatially associated granitic rocks and expand the known age range of Sn-polymetallic mineralization in southern Hunan Province.

2. The characteristic behavior of trace elements in cassiterite records changes in physicochemical conditions (e.g., temperature) of the source magma/hydrothermal fluids, which were important factors driving the precipitation of Sn-enriched minerals and were not related to fluid redox conditions. HFSE content tends to increase and its range of variation becomes more limited from quartz vein-type to skarn-type to granite-type cassiterites. Accordingly, the degree of magmatic evolution of related granites increases.

3. The magmatic emplacement and metallogenic evolution of the southern Hunan tin province can be divided into three main stages: (1) Stage I (Early Paleozoic

and Triassic): initial enrichment stage of tungsten and tin; (2) Stage II (Jurassic): metasomatic mineralization stage; and (3) Stage III (Cretaceous): magmatic-hydrothermal superposition stage. This study shows that the highly differentiated Cretaceous-age granites and their peri-plutonic areas are important targets for Sn ore exploration in the Nanling region.

ACKNOWLEDGMENTS

We are grateful to Don Baker (Editor-in-Chief), Matthew Steele-MacInnis (Associate Editor), and two reviewers (Prof. Jason Bennett and Prof. Lorenzo Tavazzani) for their constructive comments and suggestions that significantly improved this study.

FUNDING

This work was financed by the National Natural Science Foundation of China (Grant No. 92162103) and the Fundamental Research Funds for the Central Universities of Central South University (Grant No. 2021zzts0252 and No. 2022ZZTS0529).

REFERENCES CITED

Bau, M. (1996) Controls on the fractionation of isovalent trace elements in magmatic and aqueous systems: Evidence from Y/Ho, Zr/Hf, and lanthanide tetrad effect. Contributions to Mineralogy and Petrology, 123, 323–333.

Bennett, J.M., Kemp, A.I.S., and Roberts, M.P. (2020) Microstructural controls on the chemical heterogeneity of cassiterite revealed by cathodoluminescence and elemental X-ray mapping. American Mineralogist, 105, 58–76.

Brugger, J., Lahaye, Y., Costa, S., Lambert, D., and Bateman, R. (2000) Inhomogeneous distribution of REE in scheelite and dynamics of Archaean hydrothermal systems (Mt. Charlotte and Drysdale gold deposits, Western Australia). Contributions to Mineralogy and Petrology, 139, 251–264.

Cai, Y., Ma, D.S., Lu, J.J., Huang, H., Zhang, R.Q., and Qu, W.J. (2012) Re- Os geochronology and S isotope geochemistry of Dengfuxian tungsten deposit Hunan Province China. Acta Geologica Sinica, 28, 3798–3808.

Černý, P., and Ercit, T.S. (1985) Some recent advances in the mineralogy and geochemistry of Nb and Ta in rare-element granitic pegmatites. Bulletin de Mineralogie, 108, 499–532.

Černý, P., Roberts, W.L., Ercit, T.S., and Chapman, R. (2015) Wodginite and associated oxide rninerals from the Peerless pegmatite. American Mineralogist, 70, 1044-1049.

Che, X.D., Wang, R.C., Wu, F.Y., Zhu, Z.Y., Zhang, W.L., Hu, H., Xie, L., Lu, J.J., and Zhang, D. (2019) Episodic Nb–Ta mineralisation in South China: Constraints from in situ LA–ICP–MS columbite-tantalite U–Pb dating. Ore Geology Reviews, 105, 71–85.

Chen, Y.X., Li, H., Sun, W.D., Ireland, T., Tian, X.F., Hu, Y. Bin, Yang, W. Bin, Chen, C., and Xu, D.R. (2016) Generation of Late Mesozoic Qianlishan A2-type granite in Nanling Range, South China: Implications for Shizhuyuan W–Sn mineralization and tectonic evolution. Lithos, 266–267, 435–452.

Cheng, Y.B., Spandler, C., Kemp, A., Mao, J.W., Rusk, B., Hu, Y., and Blake, K. (2019) Controls on cassiterite (SnO2) crystallization: Evidence from cathodoluminescence, trace-element chemistry, and geochronology at the Gejiu Tin District. American Mineralogist, 104, 118–129.

Cohen, A.J., Adekeye, J.I.D., Hapke, B., and Partlow, D.P. (1985) Interstitial Sn^{2+} in synthetic and natural cassiterite crystals. Physics and Chemistry of Minerals, 12,

DOI: https://doi.org/10.2138/am-2022-8823. http://www.minsocam.org/

363–369.

Dong C.G. (2018) Study on granitic and metallogenic chronology and geodynamics of Xitian tin-tungsten deposit and Dengfuxian tungsten deposit in Hunan province, China, ~~p. 61-92.~~ Ph.D. thesis, University of Chinese Academy of Sciences, 61-92.

Fu, J.M., Ma, C.Q., Xie, C.F., Zhang, Y.M., and Peng, S.B. (2004) SHRIMP U-Pb zircon dating of the Jiuyishan composite granite in Hunan and its geological significance. Geotectonica et Metallogenia, 34, 370–378.

Fu, J.M., Li, H.Q., Qu, W.J., Yang, X.J., Wei, J.Q., Liu, G.Q., and Ma, L.Y. (2007) Re-Os isotope dating of the Da'ao tungsten-tin deposit in the Jiuyi Mountains, southern Hunan Province. Geology in China, 34, 651–656.

Gemmrich, L., Torró, L., Melgarejo, J.C., Laurent, O., Vallance, J., Chelle-Michou, C., and Sempere, T.P.A. (2021) Trace element composition and U-Pb ages of cassiterite from the Bolivian tin belt. Mineralium Deposita, 56, 1491–1520.

Green, T.H., and Pearson, N.J. (1987) An experimental study of Nb and Ta partitioning between Ti-rich minerals and silicate liquids at high pressure and temperature. Geochimica et Cosmochimica Acta, 51, 55–62.

Guo, C.L., Wang, R.C., Yuan, S. Da, Wu, S.H., and Yin, B. (2015) Geochronological and geochemical constraints on the petrogenesis and geodynamic setting of the Qianlishan granitic pluton, Southeast China. Mineralogy and Petrology, 109, 253–282.

Guo, J., Lu, Y., Fu, J., Qin, Z., Ning, Y., and Zhang, Z. (2019) Geology and geochronology of the Maozaishan Sn deposit, Hunan Province: constraints from zircon U–Pb and muscovite Ar–Ar dating. Minerals, 9, 14–16.

Han, Y.W., Ma, Z.D., Zhang, H.F., Zhang, B. R., Li, F.L., Gao, S., and Bao, Z.Y.

(2003) Geochemistry, Geology Press, Beijing, p. 181-188.

He, M., Liu, Q., Hou, Q.L., Sun, J.F., Zhang, J.H., Wu, S.C., and Zhu, H.F. (2018) Petrogenesis of the Dengfuxian granite, eastern Hunan Province and constraints on mineralization: Evidences from zircon and cassiterite U-Pb geochronology， zircon Hf-O isotopes and whole-rock geochemistry. Acta Geologica Sinica, 34, 637–655.

Heinrich, C.A. (1990) The chemistry of hydrothermal tin(-tungsten) ore deposition. Economic Geology, 85, 457–481.

Hennigh, Q.T., and Hutchinson, R. W. (1999) Cassiterite at Kidd Creek: an example of volcanogenic massive sulfide-hosted tin mineralization. In: Hannington, M.D., and Barrie, C.T. (eds.), The Giant Kidd Creek Volcanogenic Massive Sulfide Deposit, Western Abitibi Subprovince, Canada, Society of Economic Geologists, Economic Geology Monograph 10, Littleton, Colorado, p. 431-440.

Hu, P.C., Zhu, W.G., Zhong, H., Zhang, R.Q., Zhao, X.Y., and Mao, W. (2021) Late Cretaceous granitic magmatism and Sn mineralization in the giant Yinyan porphyry tin deposit, South China: constraints from zircon and cassiterite U–Pb and molybdenite Re–Os geochronology. Mineralium Deposita, 56, 743–765.

Hu, R.Z., Chen, W.T., Xu, D.R., and Zhou, M.F. (2017) Reviews and new metallogenic models of mineral deposits in South China: An introduction. Journal of Asian Earth Sciences, 137, 1–8.

Huang, H., Ma, D.S., Lu, J.J. Cai, Y., and Xie, X. (2011) Zircon U-Pb geochronology characteristics of Dengfuxian complex granite, Eastern Hunan Province, China. Acta Mineralogica Sinica, 33, 590–591.

Huang, H., Ma, D.S., Lu, J.J., Cai, Y., and Xie, X. (2013) Zircon U-Pb geochronology and geochemistry characteristics of Dengfuxian two-mica granite, Eastern Hunan province, China. Acta Geologica Sinica, 33, 245–255.

Jiang, S.Y., Zhao, K.D., Jiang, H., Su, H.M., Xiong, S.F., Xiong, Y., Xu, Y.M., Zhang, W., and Zhu, L.Y. (2020) Spatiotemporal distribution, geological characteristics and metallogenic mechanism of tungsten and tin deposits in China: An overview. Chinese Science Bulletin, 65, 3730–3745.

Korges, M., Weis, P., Lüders, V., and Laurent, O. (2018) Depressurization and boiling of a single magmatic fluid as a mechanism for tin-tungsten deposit formation. Geology, 46, 75–78.

Lehmann, B. (2021) Formation of tin ore deposits: A reassessment. Lithos, 402–403, 105756.

Li, H., Palinkaš, L.A., Watanabe, K., and Xi, X.S. (2018a) Petrogenesis of Jurassic A-type granites associated with Cu-Mo and W-Sn deposits in the central Nanling region, South China: Relation to mantle upwelling and intra-continental extension. Ore Geology Reviews, 92, 449–462.

Li, H., Wu, J.H., Evans, N.J., Jiang, W.C., and Zhou, Z.K. (2018b) Zircon geochronology and geochemistry of the Xianghualing A-type granitic rocks: Insights into multi-stage Sn-polymetallic mineralization in South China. Lithos, 312–313, 1–20.

Li, H., Sun, H.S., Algeo, T.J., Wu, J.H., Cao, J.Y., and Wu, Q.H. (2019) Mesozoic multi-stage W–Sn polymetallic mineralization in the Nanling Range, South China: An example from the Dengfuxian–Xitian ore field. Geological Journal, 54, 3755–3785.

Li, H.Y., and Mao, J.W. (1996) Re-Os isotopic chronology of molybdenites in the Shizhuyuan polymetallic tungsten deposit, Southern Hunan. Geological Review, 42, 261–267.

Li, J.F., Fu, J.M., Ma, C.Q., Lu, Y.Y., Cheng, S.B., Ma, L.Y., Qin, Z.W., and Sheng, H.Q. (2021) Zircon U-Pb ages, geochemical characteristics and geological significance of Jinjiling Pluton in Nanling. Earth Science (Journal of China University of Geosciences-Wuhan), 46, 1231–1247.

Li, X.H., and McCulloch, M.T. (1996) Secular variation in the Nd isotopic composition of Neoproterozoic sediments from the southern margin of the Yangtze Block: Evidence for a Proterozoic continental collision in southeast China. Precambrian Research, 76, 67–76.

Li, X.H., Liu, D.Y., Sun, M., Li, W.X., Liang, X.R., and Liu, Y. (2004) Precise Sm-Nd and U-Pb isotopic dating of the supergiant Shizhuyuan polymetallic deposit and its host granite, SE China. Geological Magazine, 141, 225–231.

Li, Y.S., Zhu, J.C., Zheng, M. gong, Wu, Y.Y., Hu, Z.D., and Zhang, G. C. (1986) Rb-Sr chronology and genesis of Jiuyishan granite complex. Uranium Geology, 2, 257–264.

Liao, Y.Z., Zhao, B., Zhang, D.H., Danyushevsky, L. V., Li, T.L., Wu, M.Q., and Liu, F. (2021) Evidence for temporal relationship between the late Mesozoic multistage Qianlishan granite complex and the Shizhuyuan W–Sn–Mo–Bi deposit, SE China. Scientific Reports, 11, 1–24.

Liu, B., Kong, H., Wu, Q.H., Chen, S.F., Li, H., Xi, X.S., Wu, J.H., and Jiang, H. (2022a) Origin and evolution of W mineralization in the Tongshanling Cu–polymetallic ore field, South China: Constraints from scheelite microstructure, geochemistry, and Nd–O isotope evidence. Ore Geology Reviews, 143.

Liu, B., Wu, Q.H., Kong, H., Xi, X.S., Jiang, J.B., Li, H., Cao, J.Y., and Tang, Y.Y. (2022b) The evolution sequence of granites in the Xitian ore field in Hunan and its tungsten–tin mineralization: constraints from zircon U–Pb dating and geochemical characteristics. Earth Science (Journal of China University of Geosciences-Wuhan), 47, 240–258.

Liu, C.Y., Xiao, W.Z., Zhang, L.J., Belousova, E.A., Rushmer, T., and Xie, F.Q. (2021) Formation of Li-Rb-Cs greisen-type deposit in Zhengchong, Jiuyishan district, South China: Constraints from whole-rock and mineral geochemistry. Geochemistry, 81, 125796.

Liu, Y., Lai, J.Q., Xiao, W.Z., Jeffrey, D., Du, R.J., Li, S.L., Liu, C.Y., Wen, C.H., and Yu, X.H. (2019) Petrogenesis and mineralization significance of two-stage A-type granites in Jiuyishan, South China: Constraints from whole-rock geochemistry, mineral composition and zircon U-Pb-Hf isotopes. Acta Geologica Sinica, 93, 874–900.

Liu, Y.M., Dai, T.M., Lu, H.Z., Xu, Y.Z., Wang, C.L., and Kang, W.Q. (1997) ^{40}Ar–^{39}Ar and Sm–Nd isotopic ages for the Qianlishan granite and its mineralization. Science in China (Series D), 27, 425–430.

Mao, J.W., Li, H.Y., and Pei, R.F. (1995) Nd-Sr isotopic and petrogenetic studies of the Qianlishan granite stock, Hunan province. Mineral Deposits, 14, 235–242.

Mao, J.W., Xie, G.Q., Guo, C.L., and Chen, Y.C. (2007) Large-scale tungsten-tin mineralization in the Nanling region, South China: Metallogenic ages and corresponding geodynamic processes. Acta Geologica Sinica, 23, 2329–2338.

Möller, P., Dulski, P., Szacki, W., Malow, G., and Riedel, E. (1988) Substitution of tin in cassiterite by tantalum, niobium, tungsten, iron and manganese. Geochimica et Cosmochimica Acta, 52, 1497–1503.

Neymark, L.A., Holm-Denoma, C.S., and Moscati, R.J. (2018) In situ LA-ICPMS U–Pb dating of cassiterite without a known-age matrix-matched reference material: Examples from worldwide tin deposits spanning the Proterozoic to the Tertiary.

Chemical Geology, 483, 410–425.

Pavlova, G.G., Palessky, S.V., Borisenko, A.S., Vladimirov, A.G., Seifert, T., and Phan, L.A. (2015) Indium in cassiterite and ores of tin deposits. Ore Geology Reviews, 66, 99–113.

Plimer, I.R., Lu, J., Kleeman, J.D. (1991) Trace and rare earth elements in cassiterite—sources of components for the tin deposits of the Mole Granite, Australia. Mineralium Deposita, 26, 267–274.

Rubin, J.N., Henry, C.D., and Price, J.G. (1993) The mobility of zirconium and other “immobile” elements during hydrothermal alteration. Chemical Geology, 110, 29–47.

Rudnick, R.L., McDonough, W.F., and Chappell, B.W. (1993) Carbonatite metasomatism in the northern Tanzanian mantle: petrographic and geochemical characteristics. Earth and Planetary Science Letters, 114, 463–475.

Schmidt, C. (2018) Formation of hydrothermal tin deposits: Raman spectroscopic evidence for an important role of aqueous Sn(IV) species. Geochimica et Cosmochimica Acta, 220, 499–511.

Schmidt, C., Romer, R.L., Wohlgemuth-Ueberwasser, C.C., and Appelt, O. (2020) Partitioning of Sn and W between granitic melt and aqueous fluid. Ore Geology Reviews, 117, 103263.

Shannon, R.D. (1976) Revised effective ionic radii and systematic studies of interatomic distances in halides and chalcogenides. Acta Crystallographica Section A: Crystal Physics, Diffraction, Theoretical and General Crystallography, 32(5), 751-767.

Song, F., Niu, Z.J., He, Y.Y., Algeo, T.J. and Yang, W.Q. (2020) Geographic proximity of Yangtze and Cathaysia blocks during the late Neoproterozoic demonstrated by detrital zircon evidence. Palaeogeography, Palaeoclimatology, Palaeoecology, 558, 109939.

Su, H.Z. (2017) The petrogenesis studies of the Mesozoic Xiangyuan tungsten-tin deposit and related granites in Hunan province, ~~p. 63-71.~~ M.S. thesis, China University of Geosciences, Beijing, 63-71.

Sui, Q.L., Zhu, H.L., Sun, S.J., Chen, D.H., Zhao, X.J., and Wang, Z.F. (2020) The geochemical behavior of tin and Late Cretaceous tin mineralization in South China. Acta Petrologica Sinica, 36, 23–34.

Sun, H.R., Zhao, Z., Yan, G.S., Lü, Z.C., Huang, Z.L., and Yu, X.F. (2018) Geological and geochronological constraints on the formation of the Jurassic Maozaishan Sn deposit, Dayishan orefield, South China. Ore Geology Reviews, 94, 212–224.

Sun, H.R., Lu, Z.C., Han, Z.R., Du, Z.Z., Zhang, X.M., and Wang, H. (2021) Genesis and geological significance of Late Jurassic high-B ore-bearing A-type granite in the Dayishan tin deposit, Hunan Province. Acta Petrologica Sinica, 37, 1749–1764.

Sun, S.S., and McDonough, W.F. (1989) Chemical and isotopic systematics of oceanic basalts: Implications for mantle composition and processes. In: Saunders, A.D. and Norry, M.J. (eds.), Magmatism in the Ocean Basins, Geological Society of London, Special Publication 42, 313–345.

Sverjensky, D.A. (1984) Europium redox equilibria in aqueous solution. Earth and Planetary Science Letters, 67, 70–78.

Taylor, R.G. (1979) Geology of Tin Deposits, Developments in Economic Geology 11, Elsevier, Netherlands, p. 471-483.

Tindle, A.G., and Breaks, F.W. (1998) Oxide minerals of the Separation Rapids rare-element granitic pegmatite group, northwestern Ontario. Canadian

Mineralogist, 36, 609–635.

Wang, L.L., Ni, P., Dai, B.Z., Li, W.S., Pan, J.Y., Cui, J.M., and Yan, G. (2020) Fluid inclusion study of the ore−bearing stockwork greisen at Shizhuyuan W−Sn−Mo−Bi deposit, Hunan. Journal of Nanjing University (Natural Science), 56, 653–665.

Wang, X., Griffin, W.L., and Chen, J. (2010) Hf contents and Zr/Hf ratios in granitic zircons. Geochemical Journal, 44, 65–72.

Wang, Z.Q., Chen, B., and Ma, X.H. (2014) In situ LA-ICP-MS U-Pb age and geochemical data of cassiterite of the Furong tin deposit, the Nanling Range: Implications for the origin and evolution of the ore-forming fluid. Chinese Science Bulletin, 59, 2505–2519 (in Chinese).

Wu, J.H., Li, H., Algeo, T.J., Jiang, W.C., and Zhou, Z.K. (2018) Genesis of the Xianghualing Sn–Pb–Zn deposit, South China: A multi-method zircon study. Ore Geology Reviews, 102, 220–239.

Wu, J.H., Kong, H., Li, H., Algeo, T.J., Yonezu, K., Liu, B., Wu, Q.H., Zhu, D.P., and Jiang, H. (2021) Multiple metal sources of coupled Cu-Sn deposits: Insights from the Tongshanling polymetallic deposit in the Nanling Range, South China. Ore Geology Reviews, 139, 104521.

Xiong, Y.Q, Shao, Y.J, Mao, J. W, Wu, S.C, Zhou, H.D., and Zheng, M.H. (2019) The polymetallic magmatic-hydrothermal Xiangdong and Dalong systems in the W–Sn–Cu–Pb–Zn–Ag Dengfuxian orefield, SE China: constraints from geology, fluid inclusions, H–O–S–Pb isotopes, and sphalerite Rb–Sr geochronology. Mineralium Deposita, 54, 1101–1124.

Xiong, Y.Q., Shao, Y.J., Cheng, Y.B., and Jiang, S.Y. (2020) Discrete Jurassic and Cretaceous mineralization events at the Xiangdong W(-Sn) deposit, Nanling

Range, South China. Economic Geology, 115, 385–413.

Yang, L.Z., Wu, X. Bin, Cao, J.Y., Hu, B., Zhang, X.W., Gong, Y.S., and Liu, W.D. (2018) Geochronology, petrology, and genesis of two granitic plutons of the Xianghualing ore field in South Hunan Province: constraints from zircon U–Pb dating, geochemistry, and Lu–Hf isotopic compositions. Minerals, 8, no. 213.

Yao, Y., Chen, J., Lu, J.J., Wang, R.C., and Zhang, R.Q. (2014) Geology and genesis of the Hehuaping magnesian skarn-type cassiterite-sulfide deposit, Hunan Province, Southern China. Ore Geology Reviews, 58, 163–184.

Yin, J.W., Kim, S.J., Lee, H.K., and Itaya, T. (2002) K-Ar ages of plutonism and mineralization at the Shizhuyuan W-Sn-Bi-Mo deposit, Hunan Province, China. Journal of Asian Earth Sciences, 20, 151–155.

Yu, J.M., and Jiang, S.Y. (2001) Trace element geochemistry of cassiterite from the Neves Corvo massive sulfide deposit, Portugal. Geochimica, 30, 140–146.

Yuan, S.D., Peng, J.T., Shen, N.P., Hu, R.Z., and Dai, T.M. (2007) ^{40}Ar-^{39}Ar isotopic dating of the Xianghualing Sn-polymetallic orefield in southern Hunan, China and its geological implications. Acta Geologica Sinica (English Edition), 81, 278–286.

Yuan, S.D., Peng, J., Hu, R., Li, H., Shen, N., and Zhang, D. (2008) A precise U-Pb age on cassiterite from the Xianghualing tin-polymetallic deposit (Hunan, South China). Mineralium Deposita, 43, 375–382.

Yuan, S.D., Peng, J.T., Hao, S., Li, H.M., Geng, J.Z., and Zhang, D.L. (2011) In situ LA-MC-ICP-MS and ID-TIMS U-Pb geochronology of cassiterite in the giant Furong tin deposit, Hunan Province, South China: New constraints on the timing of tin-polymetallic mineralization. Ore Geology Reviews, 43, 235–242.

Yuan S.D., Mao J.W., Cook N.J., Wang X.D., Liu X.F., and Yuan Y.B. (2015) A Late

Cretaceous tin metallogenic event in Nanling W-Sn metallogenic province: Constraints from U-Pb, Ar-Ar geochronology at the Jiepailing Sn-Be-F deposit, Hunan, China. Ore Geology Reviews, 65, 283-293.

Yuan, S.D., Williams-Jones, A.E., Mao, J.W., Zhao, P.L., Yan, C., and Zhang, D.L. (2018) The origin of the Zhangjialong tungsten deposit, south China: Implications for W-Sn mineralization in large granite batholiths. Economic Geology, 113, 1193–1208.

Zeng, Z.F. (2013) Research on Tectonic Ore-Controlling and Metallogenic Mechanism of the Dayishan Tin Field, Hunan, China, ~~p. 47-50.~~ Ph.D. thesis, China University of Geosciences, Wuhan, 47-50

Zhang, D.L., Peng, J.T., Hu, R. zhong, Yuan, S. Da, and Zheng, D.S. (2011) The closure of U-Pb isotope system in cassiterite and its reliability for dating. Geological Review, 57, 549–554.

Zhang, X., Luo, H., Wu, Z., Fan, X., Xiong, J., Yang, J., and Mou, J. (2014) Rb-Sr isochron age and its geological significance of Baishaziling tin deposit in Dayishan ore field, Hunan Province. Earth Science (Journal of China University of Geosciences), 39, 1322–1332.

Zhang, Z.Z., Ning, Y.Y., Lu, Y.Y., Cao, J.Y., Fu, J.M., Zhao, Z., Guo, J., Ma, L.Y., Qin, Z.W., and Li, J.F. (2021) Geological characteristics and metallogenic age of Tengshan'ao Sn deposit in Dayishan of South Hunan and its prospecting significance. Solid Earth Sciences, 6, 37–49.

Zhao, Z., Yang, X.Y., Zhang, T.Y., Lu, Y.Y., Li, W.Y., and Zhang, Z.Z. (2022a) Geochemical characteristics and boron isotopes of tourmaline from the Baishaziling tin deposit, Nanling Range: Constraints on magmatic-hydrothermal processes. Ore Geology Reviews, 142, 104695.

Zhao, Z., Yang, X., Lu, Y., Zhang, Z., Chen, S., Sun, C., Hou, Q., Wang, Y., and Li, S. (2022b) vein system in Dayishan pluton, Southern China: Implications for potential mineralization. American Mineralogist, 107, 495–508.

Zhao, Z.X., Xu, Z.W., Zuo, C.H., Lu, J.J., Wang, R.C., Miao, B.H., and Lu, R. (2017) Emplacement Time and Material Source of the Southern Dayishan Granitic Batholith (Taipingshan Body), Guiyang City, Hunan Province. Geological Review, 63, 395-412.

Zhu, D.P., Li, H., Algeo, T.J., Jiang, W.C., and Wang, C. (2021) The prograde-to-retrograde evolution of the Huangshaping skarn deposit (Nanling Range, South China). Mineralium Deposita, 56, 1087–1110.

Zhu, X.Y., Wang, J. Bin, Wang, Y.L., and Chen, X.Y. (2015) The role of magma-hydrothermal transition fluid in the skarn-type tungsten mineralization process: A case study from the Shizhuyuan tungsten and tin polymetallic ore deposit. Acta Geologica Sinica, 31, 892–905.

Zhu, Y.N., Peng, J.T., Liu, S.Y., and Sun, Y.Z. (2014) Mineral deposit geology and trace element geochemistry of wolframite from the Woxi deposit, western Hunan, China. Geochimica, 43, 287–300.

DOI: https://doi.org/10.2138/am-2022-8823. http://www.minsocam.org/

Figure captions

Fig. 1. (a) Sketch map showing the main terranes of China (modified after Wu et al. 2018); (b) Geological map of South China Craton (modified after Yuan et al. 2018); (c) Geologic map of the Nanling Range showing the age distribution of granites and spatially associated tungsten/tin deposits (modified after Mao et al. 2007; Yuan et al. 2018, 2019).

Fig. 2. Simplified geological maps of study areas of five tin deposits: (a) Dengfuxian (after internal data from 214 Geological Team of Hunan Province, 2010, and Xiong et al. 2020b); (b) Xianghualing (after Wu et al. 2018); (c) Dayishan (after Sun et al. 2018 and Zeng 2013); (d) Shizhuyuan (after Liao et al. 2021); (e) Jiuyishan (after Li et al. 2019, 2021).

Fig. 3. Field pictures and hand specimen photomicrographs from five tin deposits. (a) Sulfide-bearing wolframite quartz veins at DFX; (b) and (c) hand specimens of sulfide-bearing wolframite quartz vein; (d) greisen-quartz veins at DYS; (e) and (f) hand specimens of greisen-quartz veins; (g) skarn-greisen network veins at SZY; (h) and (i) hand specimens of skarn-greisen network veins; (j) biotite granite at XHL; (k) and (l) hand specimens of granite; (m) to (o) greisen veins at JYS. Mineral abbreviations: Py = pyrite, Cst = cassiterite, Grt = garnet, Bt = biotite.

Fig. 4. Transmitted light photomicrographs of cassiterite grains from five tin deposits, (a, c, e, g, i plane-polarized transmitted light; b, d, f, h, j cross-polarized transmitted light). DFX (a-b): Semi-idiomorphic cassiterite crystallized in quartz vein; DYS (c-d):

Metasomatic cassiterite in greisen vein; SZY (e-f): Cassiterite crystallized in greisen skarn vein with obvious metasomatism; XHL (g-h): Semi-idiomorphic cassiterite crystallized in granite; JYS (i-j): Semi-idiomorphic cassiterite crystallized in greisen. Mineral abbreviations: Qtz = quartz, Cst = cassiterite, Ms = muscovite, Bt = biotite.

Fig. 5. Cathodoluminescence (CL) images of cassiterites from five tin deposits: (a) DFX; (b) DYS; (c) SZY; (d) XHL; and (e) JYS.

Fig. 6. Tera–Wasserburg concordia diagrams for cassiterite grains from five tin deposits: (a) DFX, (b) DYS, (c) SZY, (d) XHL, and (e) JYS.

Fig. 7. Geochronologic chart of Sn-ore mineralization and related granites in southern Hunan Province, including the new U-Pb cassiterite data of the present study.

Fig. 8. Plots of selected trace elements in cassiterite grains from five tin deposits: (a) Nb+Ta vs Fe+Mn in cassiterite (modified from Tindle and Breaks 1998); (b) Fe vs W in cassiterite (analyzed by LA–ICP–MS). The granite-related tin deposits field is based on data from Hennigh and Hutchinson (1999); Wang et al. (2014); and Pavlova et al. (2015), and the VMS/SEDEX tin deposits field is from Hennigh and Hutchinson (1999). The dashed line represents the approximate detection limit for W by PIXE probe (Hennigh and Hutchinson 1999).

Fig. 9. Log-scale scatter plots of selected trace elements for cassiterite grains from five tin deposits: (a) Nb vs Ta, (b) Zr vs Hf, (c) Zr/Hf vs Nb/Ta; (d) Fe vs W, (e) Zr vs Ti, and (f) Fe vs Nb+Ta. Sources: Guo et al. 2018; Chen et al. 2019; Cheng et al. 2019;

Hu et al. 2021; Wu et al. 2021.

Fig. 10. Log-scale scatter plots of U and Ti content for cassiterite grains and associated granite from five tin deposits: (a) Ti content, (b) U content. Sources: Li et al. 2019; Sun et al. 2021; Liao et al. 2021; Yang et al. 2018; Liu et al. 2019; Li et al. 2021.

Fig. 11. Chondrite-normalized REE patterns for southern Hunan cassiterite-hosted tin deposits (normalization after Sun and McDonough 1989). (a) DFX, (b) DYS, (c) SZY, (d) XHL, (e) JYS, and (f) all samples. Data for quartz vein-type cassiterite in the Tongshanling deposit (Wu et al. 2021) is included for reference.

Fig. 12. Score graph and loading graph of principal component analysis (PCA) of cassiterite from southern Hunan Province.

Fig. 13. Score plot of the orthogonal projection to latent structures-discriminant analysis (OPLS-DA) models between the five tin deposits. (a) DFX vs. DYS, (b) DFX vs. SZY, (c) DFX vs. XHL, (d) DFX vs. JYS, (e) SZY vs. XHL, (f) SZY vs. JYS, (g) DYS vs. JYS, (h) DYS vs. SZY, and (i) DYS vs. XHL.

Fig. 14. Diagenesis and mineralization model diagram of Sn polymetallic deposits in southern Hunan Province. (a) Schematic diagram of the multistage magmatic-hydrothermal evolution developed from previously reported data (Li et al. 2018a; Luo et al. 2022; Liu et al. 2022b) and the results of this study, and (b) ideal tin metallogenic model diagram (inspired by Gemmrich et al. 2021).

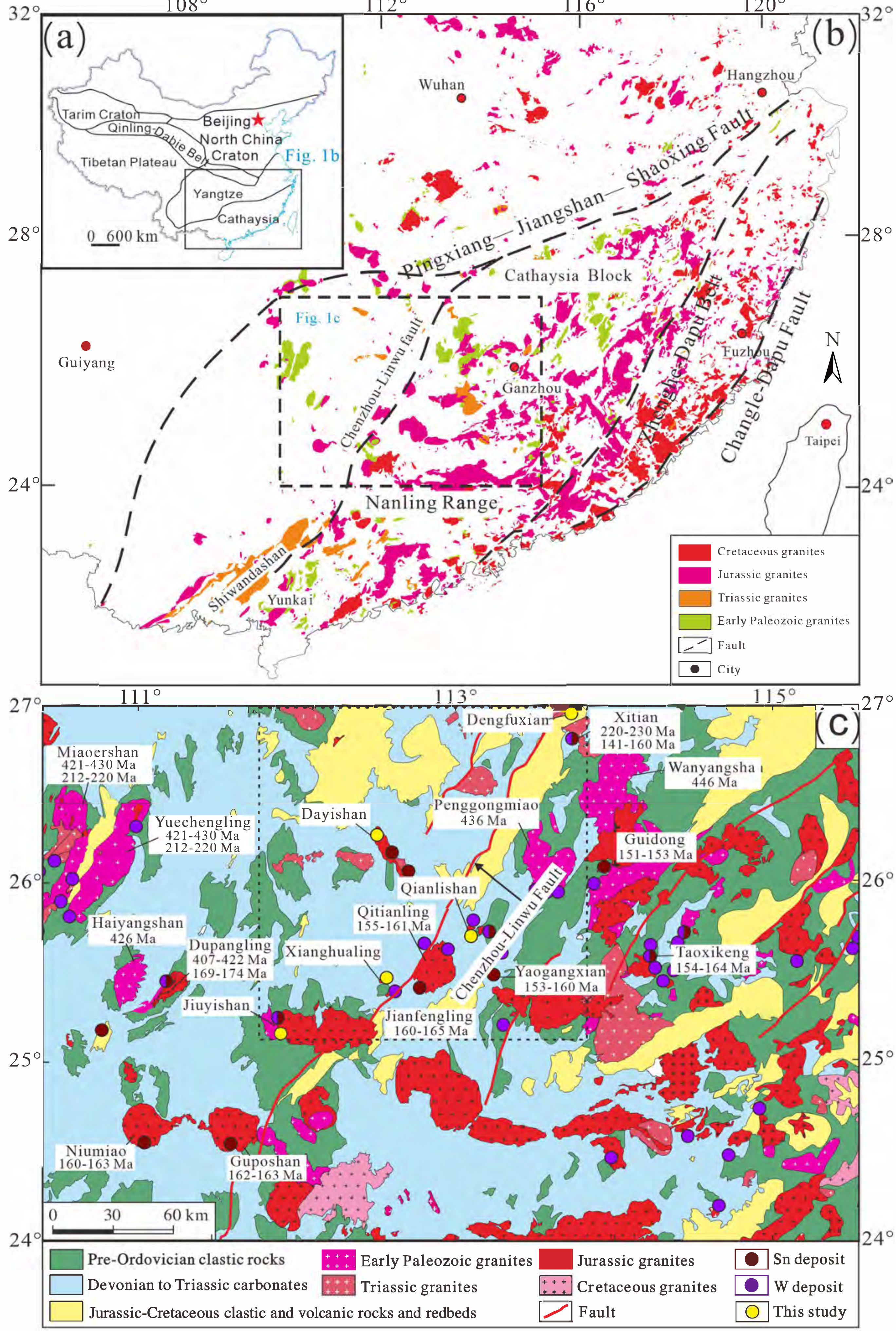

(a)
Tarim Craton
Qinling-Dabie Belt
Beijing
North China Craton
Tibetan Plateau
Fig. 1b
Yangtze
Cathaysia
0 600 km
(b)
108°
112°
116°
120°
32°
28°
24°
Wuhan
Hangzhou
Pingxiang—Jiangshan—Shaoxing Fault
Cathaysia Block
Fig. 1c
Chenzhou-Linwu fault
Zhenghe-Dapu Belt
Changle-Dapu Fault
Guiyang
Ganzhou
Fuzhou
Taipei
N
Nanling Range
Shiwandashan
Yunkai
Cretaceous granites
Jurassic granites
Triassic granites
Early Paleozoic granites
Fault
City
(c)
111°
113°
115°
27°
26°
25°
24°
Dengfuxian
Xitian
220-230 Ma
141-160 Ma
Miaoershan
421-430 Ma
212-220 Ma
Wanyangshan
446 Ma
Penggongmiao
436 Ma
Dayishan
Yuechengling
421-430 Ma
212-220 Ma
Guidong
151-153 Ma
Qianlishan
Haiyangshan
426 Ma
Qitianling
155-161 Ma
Dupangling
407-422 Ma
169-174 Ma
Xianghualing
Chenzhou-Linwu Fault
Taoxikeng
154-164 Ma
Yaogangxian
153-160 Ma
Jiuyishan
Jianfengling
160-165 Ma
Niumiao
160-163 Ma
Guposhan
162-163 Ma
0 30 60 km
Pre-Ordovician clastic rocks
Devonian to Triassic carbonates
Jurassic-Cretaceous clastic and volcanic rocks and redbeds
Early Paleozoic granites
Triassic granites
Jurassic granites
Cretaceous granites
Fault
Sn deposit
W deposit
This study

Figure 1

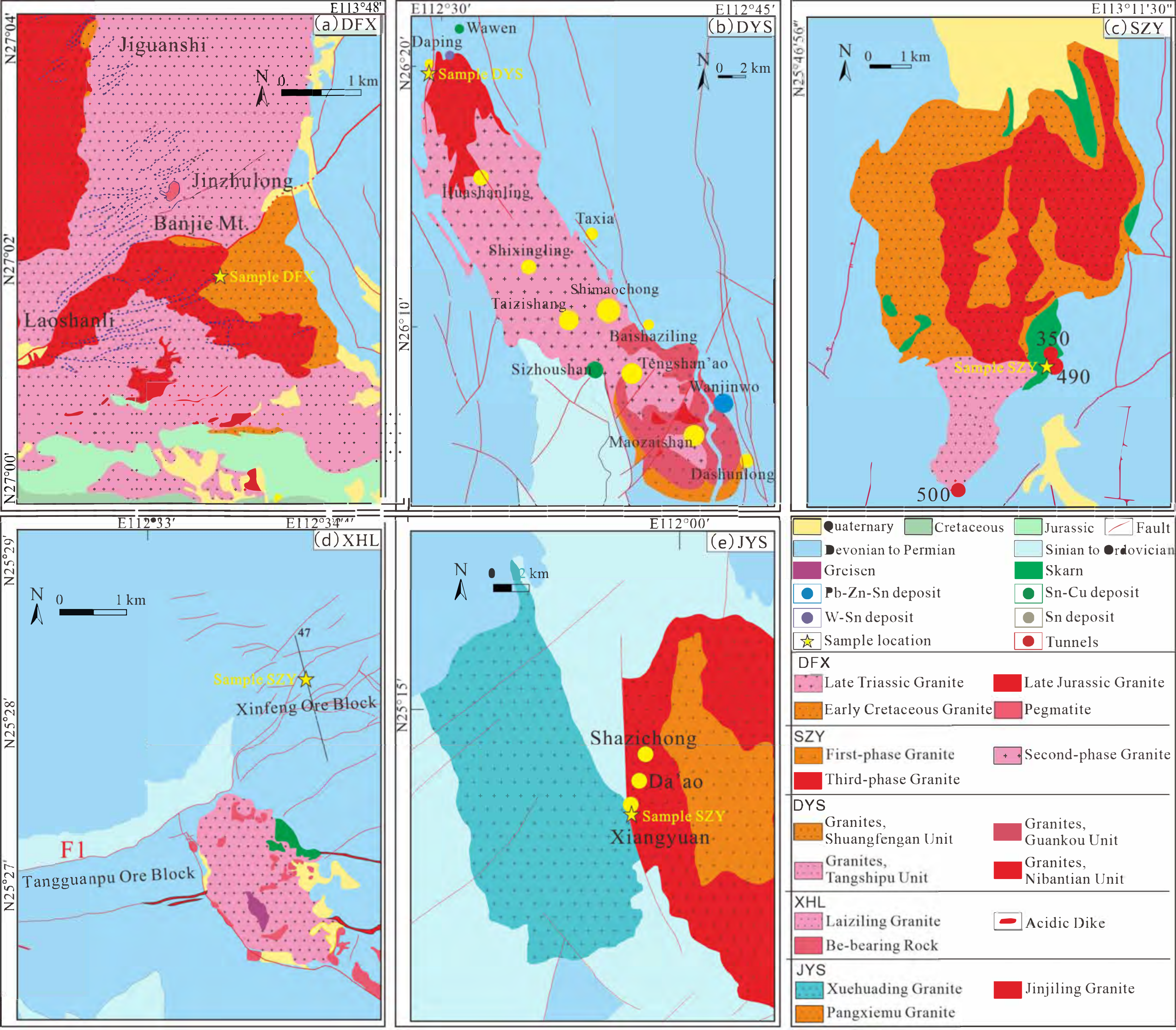

(a) DFX
E113°48'
N27°04'
N27°02'
N27°00'
Jiguanshi
Jinzhulong
Banjie Mt.
Sample DFX
Laoshanli
N
0
1 km
(b) DYS
E112°30′
E112°45′
N26°20′
N26°10′
Wawen
Daping
Sample DYS
Huashanling
Taxia
Shixingling
Shimaochong
Taizishang
Baishaziling
Sizhoushan
Tengshan'ao
Wanjinwo
Maozaishan
Dashunlong
N
0
2 km
(c) SZY
E113°11'30"
N25°46'56"
N
0
1 km
350
Sample SZY
490
500
(d) XHL
E112°33′
E112°34′
N25°29′
N25°28′
N25°27′
N
0
1 km
47
Sample SZY
Xinfeng Ore Block
F1
Tangguanpu Ore Block
(e) JYS
E112°00′
N25°15′
N
2 km
Shazichong
Da'ao
Sample SZY
Xiangyuan
Quaternary
Cretaceous
Jurassic
Fault
Devonian to Permian
Sinian to Ordovician
Greisen
Skarn
Pb-Zn-Sn deposit
Sn-Cu deposit
W-Sn deposit
Sn deposit
Sample location
Tunnels
DFX
Late Triassic Granite
Late Jurassic Granite
Early Cretaceous Granite
Pegmatite
SZY
First-phase Granite
Second-phase Granite
Third-phase Granite
DYS
Granites, Shuangfengan Unit
Granites, Guankou Unit
Granites, Tangshipu Unit
Granites, Nibantian Unit
XHL
Laiziling Granite
Acidic Dike
Be-bearing Rock
JYS
Xuehuading Granite
Jinjiling Granite
Pangxiemu Granite

Figure 2

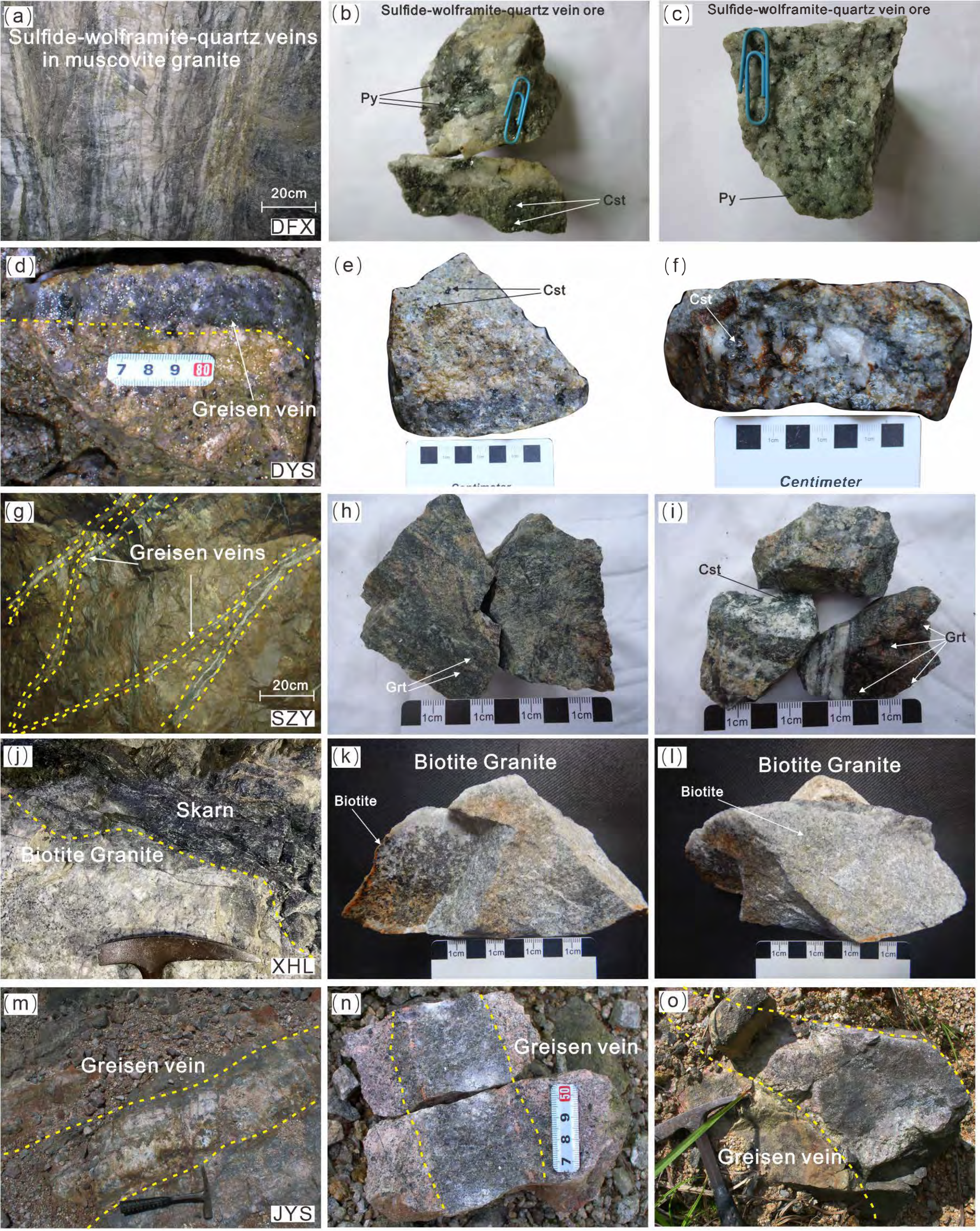
(a)
Sulfide-wolframite-quartz veins in muscovite granite
20cm
DFX
(b)
Sulfide-wolframite-quartz vein ore
Py
Cst
(c)
Sulfide-wolframite-quartz vein ore
Py
(d)
7 8 9 80
Greisen vein
DYS
(e)
Cst
(f)
Cst
Centimeter
(g)
Greisen veins
20cm
SZY
(h)
Grt
1cm
(i)
Cst
Grt
1cm
(j)
Skarn
Biotite Granite
XHL
(k)
Biotite Granite
Biotite
1cm
(l)
Biotite Granite
Biotite
1cm
(m)
Greisen vein
JYS
(n)
Greisen vein
50 9 8 7
(o)
Greisen vein

Figure 3

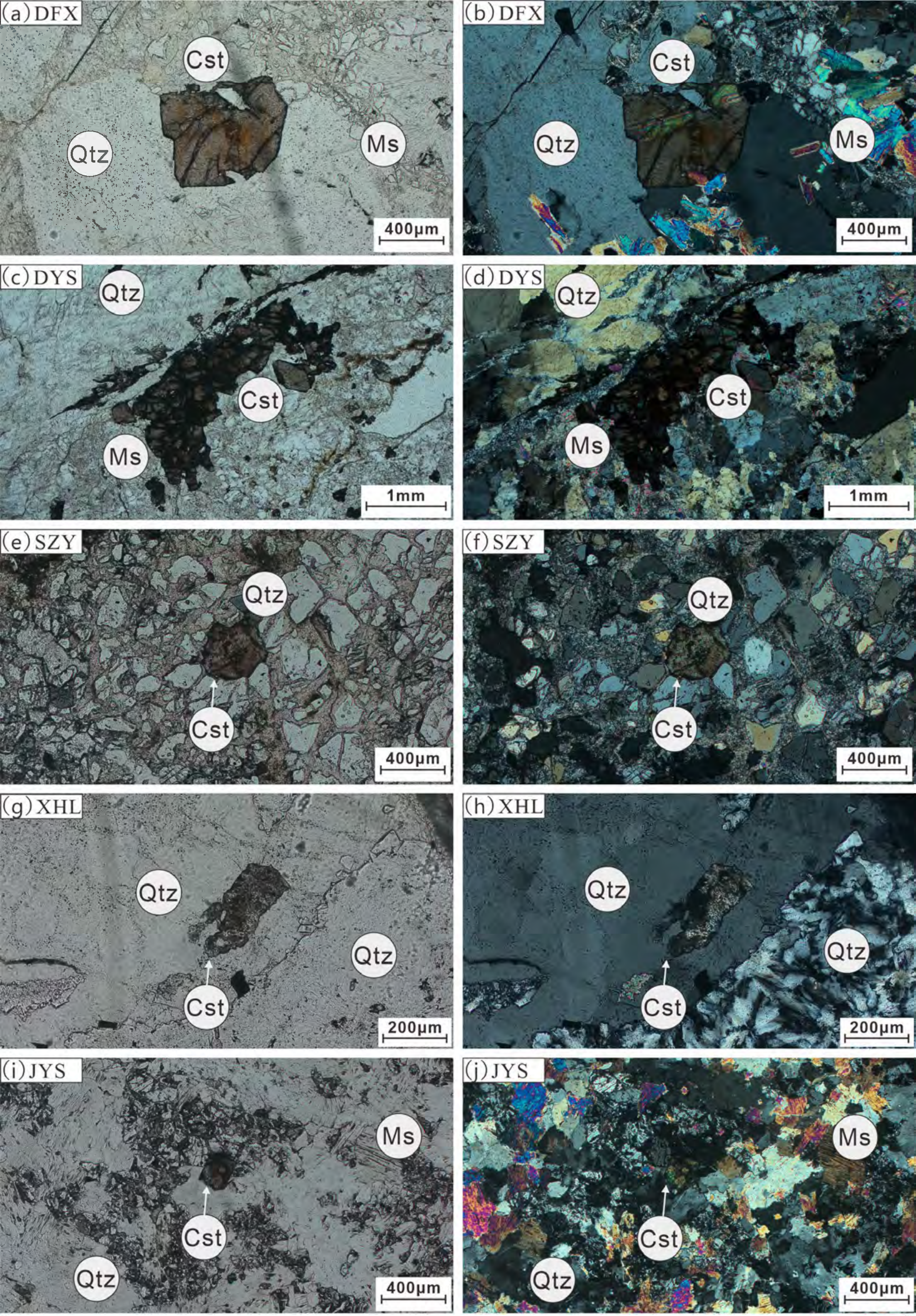
(a) DFX
Cst
Qtz
Ms
400μm
(b) DFX
Cst
Qtz
Ms
400μm
(c) DYS
Qtz
Cst
Ms
1mm
(d) DYS
Qtz
Cst
Ms
1mm
(e) SZY
Qtz
Cst
400μm
(f) SZY
Qtz
Cst
400μm
(g) XHL
Qtz
Qtz
Cst
200μm
(h) XHL
Qtz
Qtz
Cst
200μm
(i) JYS
Ms
Cst
Qtz
400μm
(j) JYS
Ms
Cst
Qtz
400μm

Figure 4

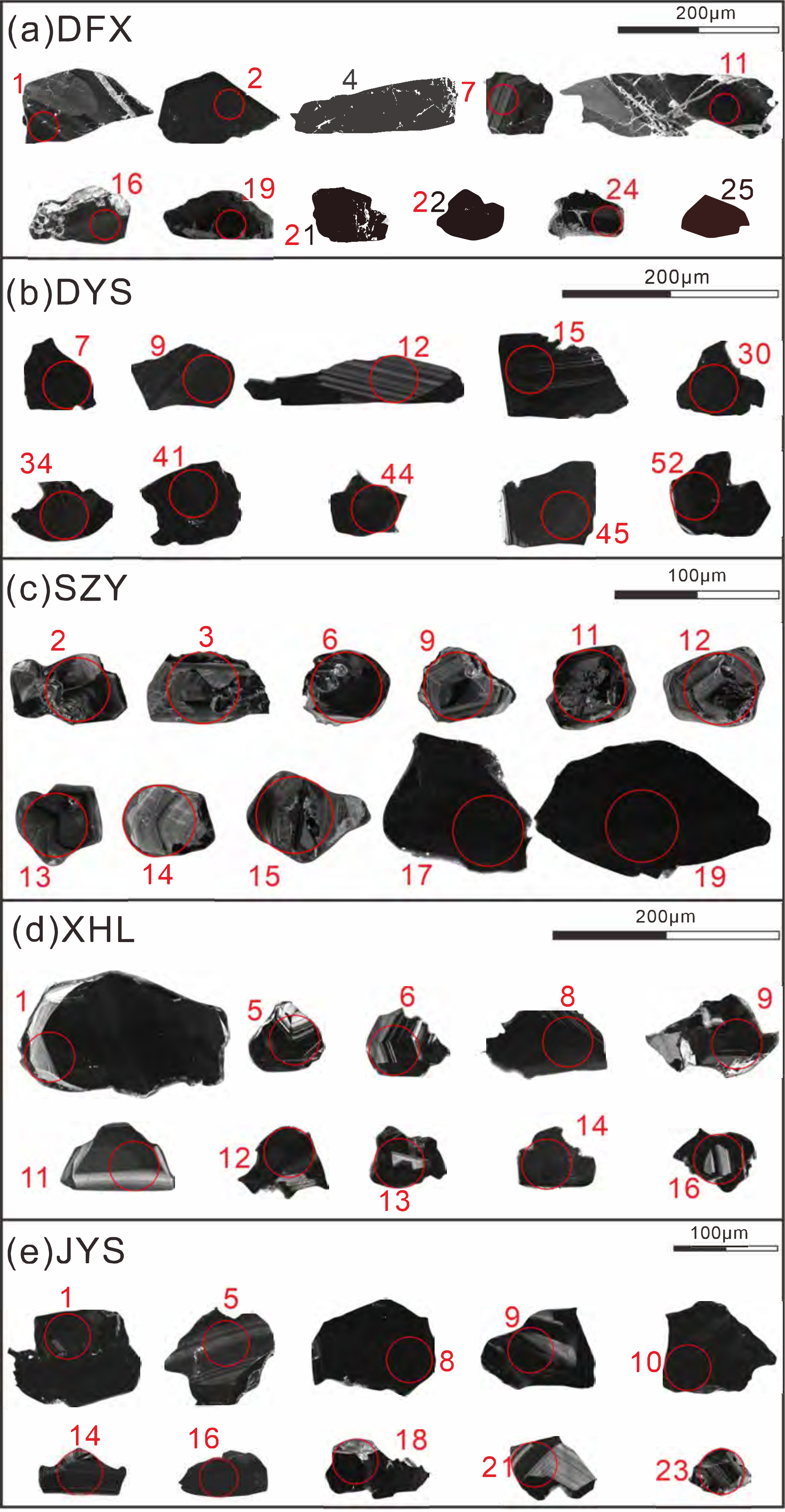
(a)DFX
200μm
1
2
4
7
11
16
19
21
22
24
25
(b)DYS
200μm
7
9
12
15
30
34
41
44
45
52
(c)SZY
100μm
2
3
6
9
11
12
13
14
15
17
19
(d)XHL
200μm
1
5
6
8
9
11
12
13
14
16
(e)JYS
100μm
1
5
8
9
10
14
16
18
21
23

Figure 5

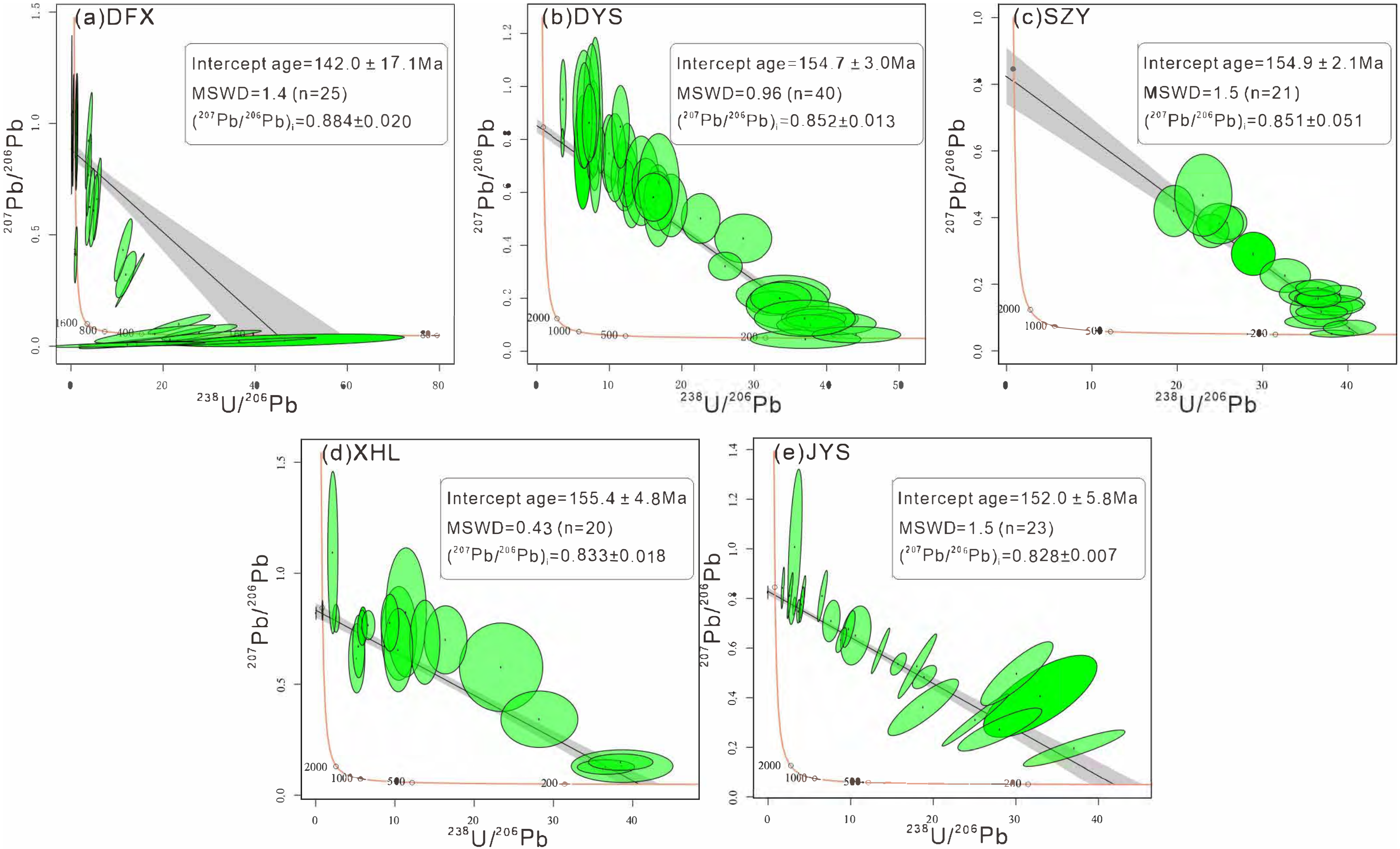

(a)DFX
Intercept age=142.0 ± 17.1Ma
MSWD=1.4 (n=25)
$(^{207}Pb/^{206}Pb)_i$=0.884±0.020
(b)DYS
Intercept age=154.7 ± 3.0Ma
MSWD=0.96 (n=40)
$(^{207}Pb/^{206}Pb)_i$=0.852±0.013
(c)SZY
Intercept age=154.9 ± 2.1Ma
MSWD=1.5 (n=21)
$(^{207}Pb/^{206}Pb)_i$=0.851±0.051
(d)XHL
Intercept age=155.4 ± 4.8Ma
MSWD=0.43 (n=20)
$(^{207}Pb/^{206}Pb)_i$=0.833±0.018
(e)JYS
Intercept age=152.0 ± 5.8Ma
MSWD=1.5 (n=23)
$(^{207}Pb/^{206}Pb)_i$=0.828±0.007
$^{207}Pb/^{206}Pb$
$^{238}U/^{206}Pb$

Figure 6

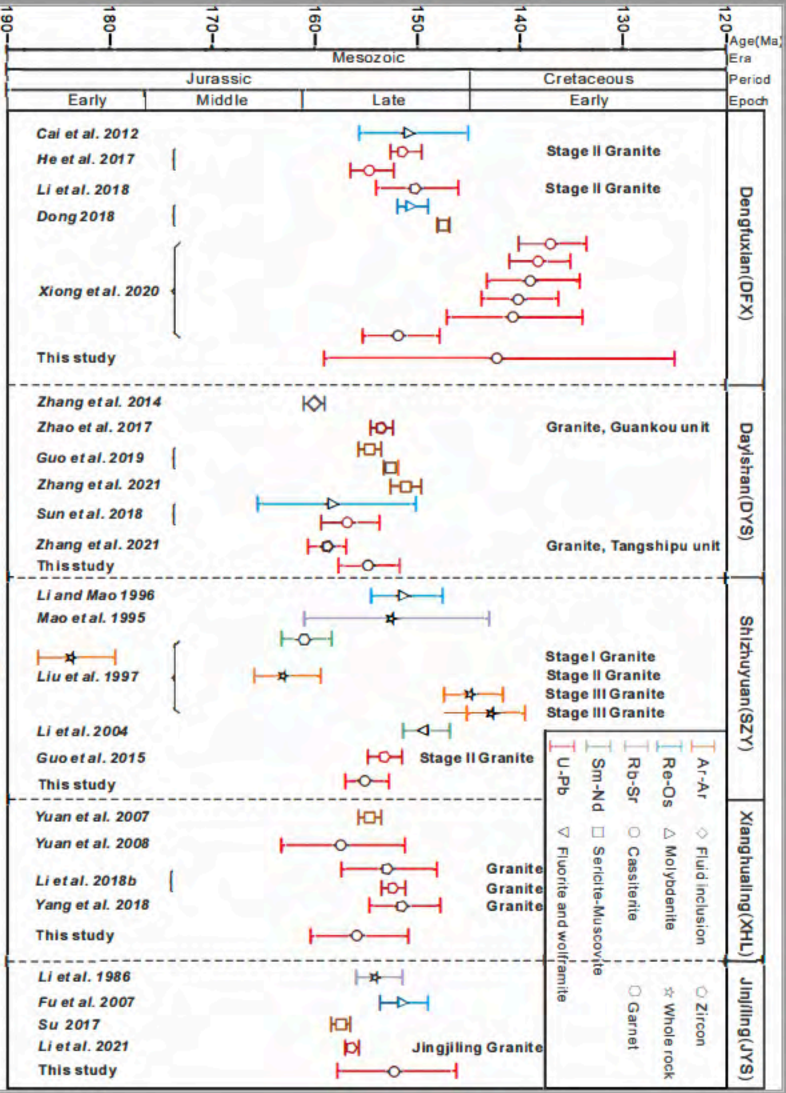

190
180
170
160
150
140
130
120
Age(Ma)
Era
Period
Epoch
Mesozoic
Jurassic
Cretaceous
Early
Middle
Late
Early
Cai et al. 2012
He et al. 2017
Li et al. 2018
Dong 2018
Xiong et al. 2020
This study
Stage II Granite
Stage II Granite
Dengfuxian(DFX)
Zhang et al. 2014
Zhao et al. 2017
Guo et al. 2019
Zhang et al. 2021
Sun et al. 2018
Zhang et al. 2021
This study
Granite, Guankou unit
Granite, Tangshipu unit
Dayishan(DYS)
Li and Mao 1996
Mao et al. 1995
Liu et al. 1997
Li et al. 2004
Guo et al. 2015
This study
Stage I Granite
Stage II Granite
Stage III Granite
Stage III Granite
Stage II Granite
Shizhuyuan(SZY)
Yuan et al. 2007
Yuan et al. 2008
Li et al. 2018b
Yang et al. 2018
This study
Granite
Granite
Granite
Xianghualing(XHL)
Li et al. 1986
Fu et al. 2007
Su 2017
Li et al. 2021
This study
Jingjiling Granite
Jinjiling(JYS)
Ar-Ar
Re-Os
Rb-Sr
Sm-Nd
U-Pb
Fluid inclusion
Molybdenite
Cassiterite
Sericite-Muscovite
Fluorite and wolframite
Zircon
Whole rock
Garnet

Figure 7

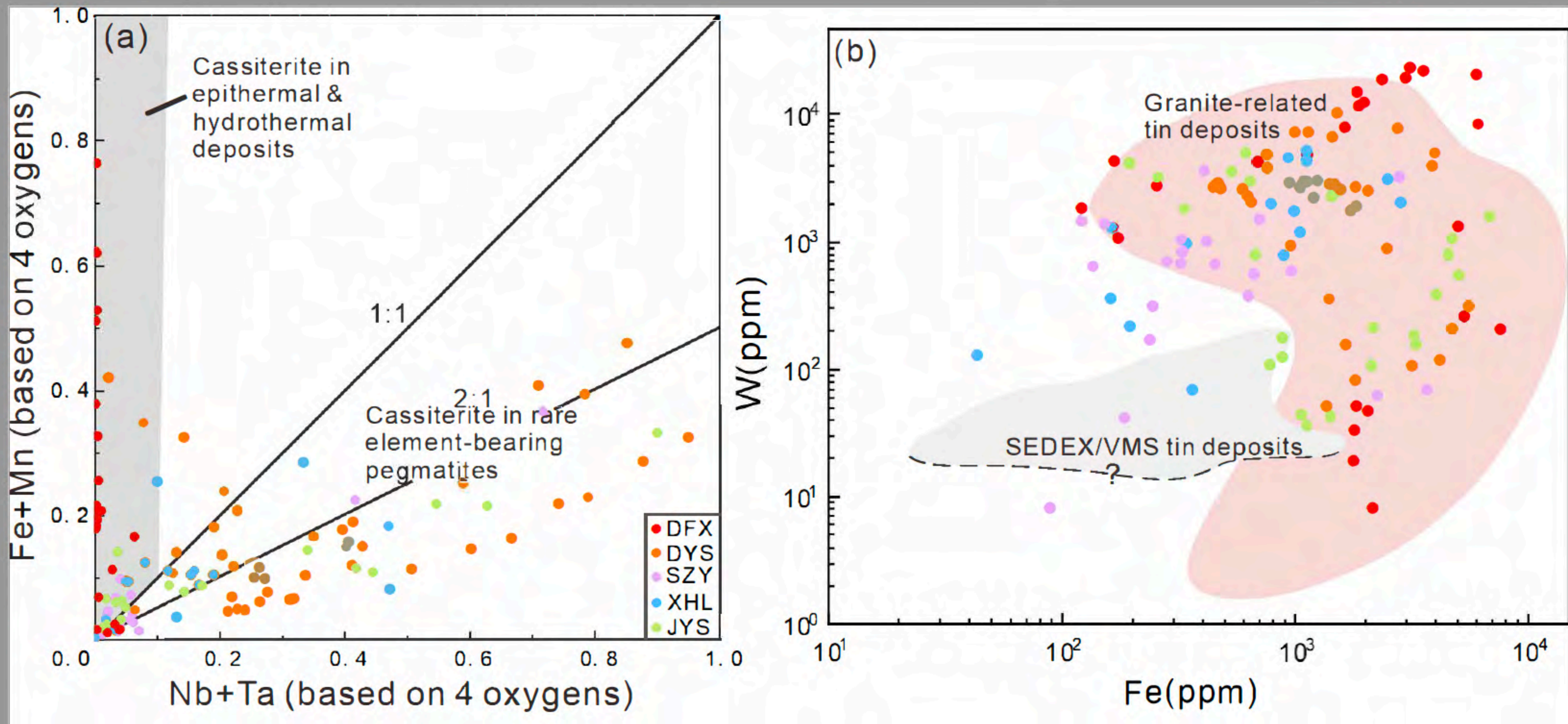

(a)
Cassiterite in epithermal & hydrothermal deposits
1:1
2:1
Cassiterite in rare element-bearing pegmatites
DFX
DYS
SZY
XHL
JYS
Fe+Mn (based on 4 oxygens)
Nb+Ta (based on 4 oxygens)
(b)
Granite-related tin deposits
SEDEX/VMS tin deposits
?
W(ppm)
Fe(ppm)

Figure 8

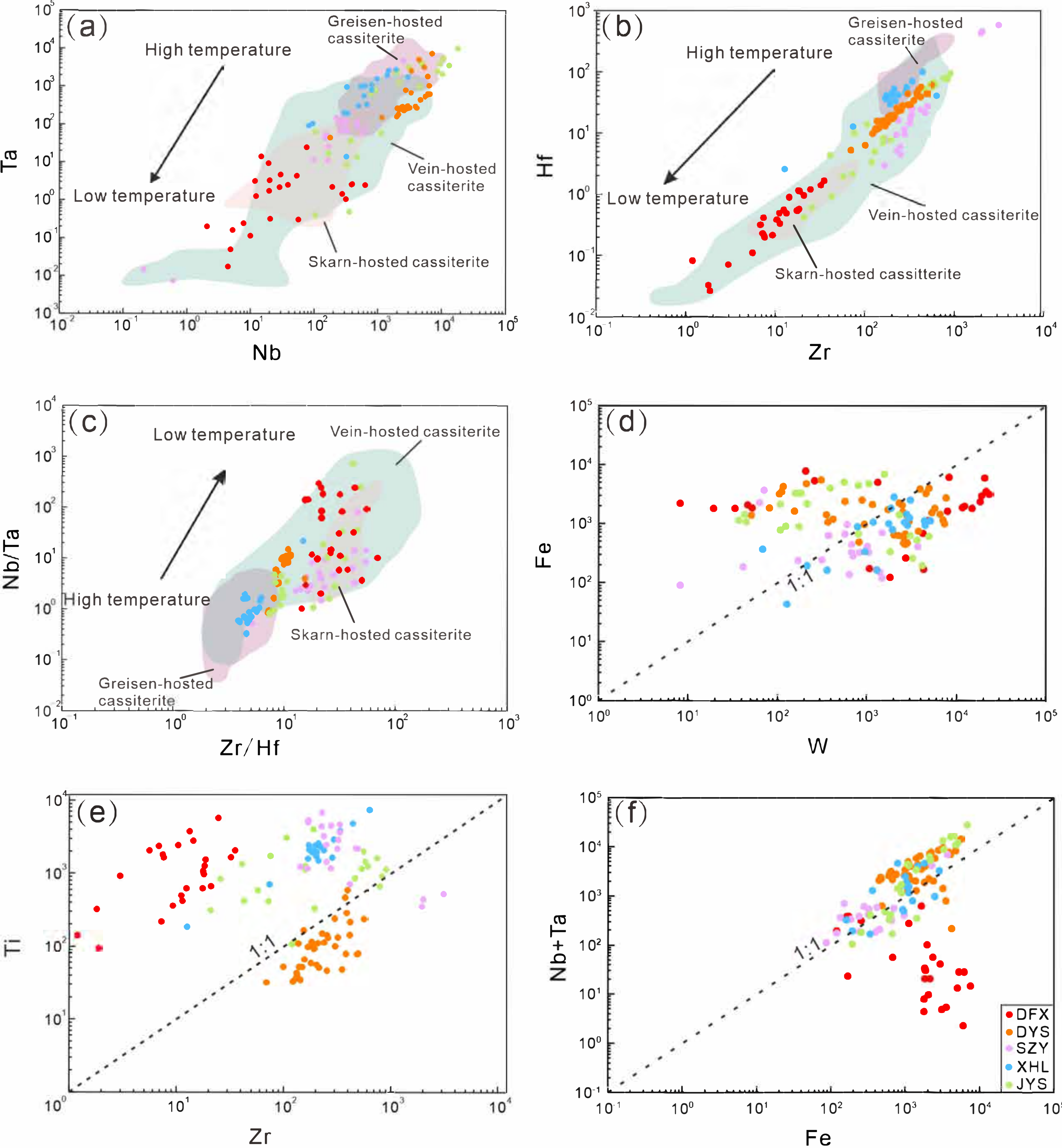
(a)
High temperature
Low temperature
Greisen-hosted cassiterite
Vein-hosted cassiterite
Skarn-hosted cassiterite
Ta
Nb
(b)
High temperature
Low temperature
Greisen-hosted cassiterite
Vein-hosted cassiterite
Skarn-hosted cassitterite
Hf
Zr
(c)
Low temperature
High temperature
Vein-hosted cassiterite
Skarn-hosted cassiterite
Greisen-hosted cassiterite
Nb/Ta
Zr/Hf
(d)
1:1
Fe
W
(e)
1:1
Ti
Zr
(f)
1:1
DFX
DYS
SZY
XHL
JYS
Nb+Ta
Fe

Figure 9

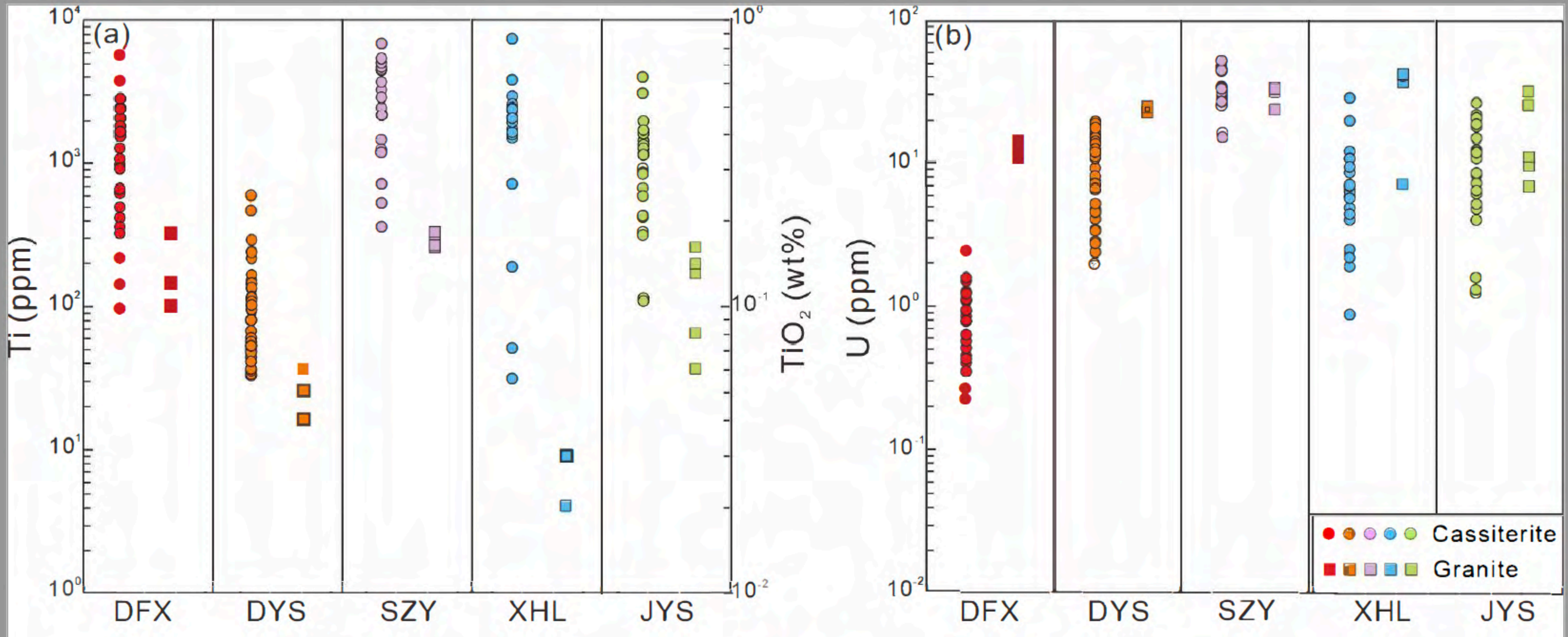

(a)
Ti (ppm)
TiO2 (wt%)
DFX
DYS
SZY
XHL
JYS
(b)
U (ppm)
Cassiterite
Granite

Figure 10

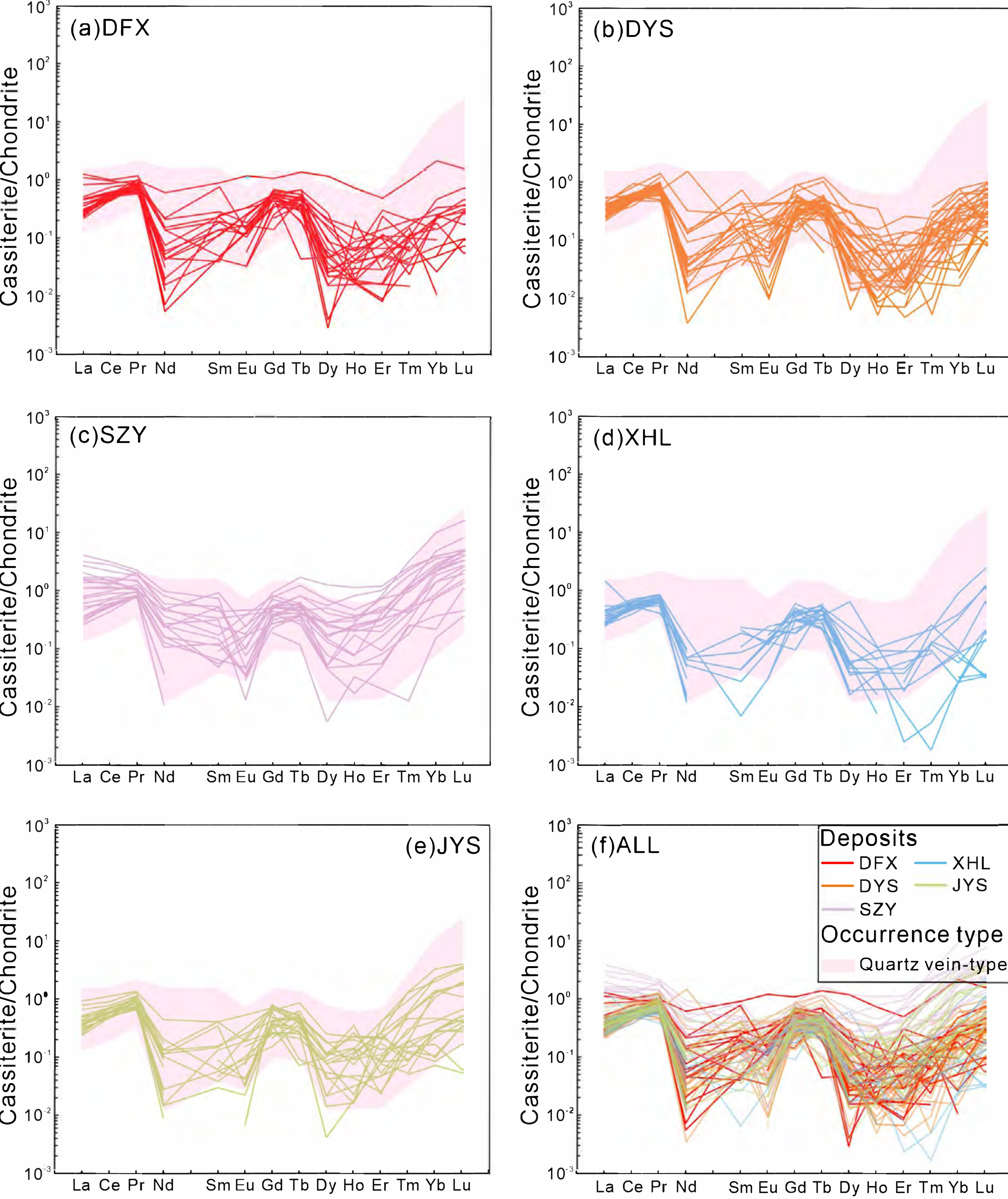
(a)DFX
(b)DYS
(c)SZY
(d)XHL
(e)JYS
(f)ALL
Cassiterite/Chondrite
10^{-3}
10^{-2}
10^{-1}
10^{0}
10^{1}
10^{2}
10^{3}
La Ce Pr Nd Sm Eu Gd Tb Dy Ho Er Tm Yb Lu
Deposits
DFX
XHL
DYS
JYS
SZY
Occurrence type
Quartz vein-type

Figure 11

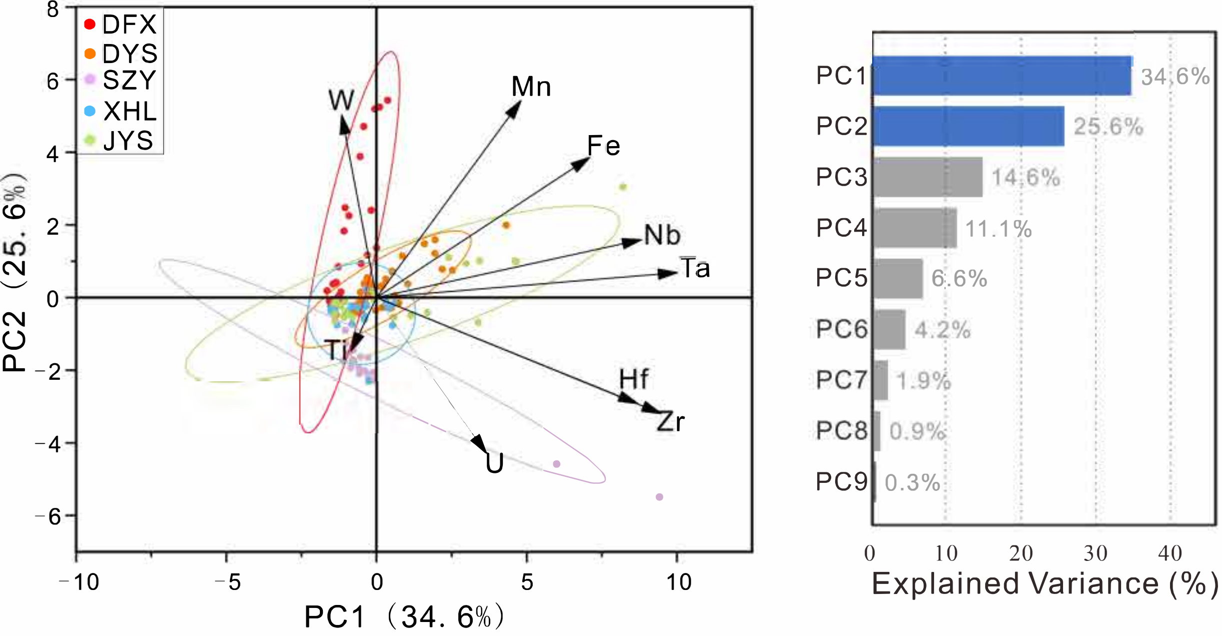

Loadings	PC1	PC2	PC3	PC4
LN(Ti)	-0.038	-0.137	0.603	0.589
LN(Mn)	0.227	0.518	0.342	-0.015
LN(Fe)	0.338	0.369	-0.043	0.076
LN(Zr)	0.457	-0.299	0.124	-0.306
LN(Nb)	0.425	0.166	-0.263	0.335
LN(Hf)	0.419	-0.276	0.111	-0.443
LN(Ta)	0.481	0.073	-0.170	0.285
LN(W)	-0.061	0.472	0.455	-0.385
LN(U)	0.181	-0.395	0.430	0.122

Figure 12

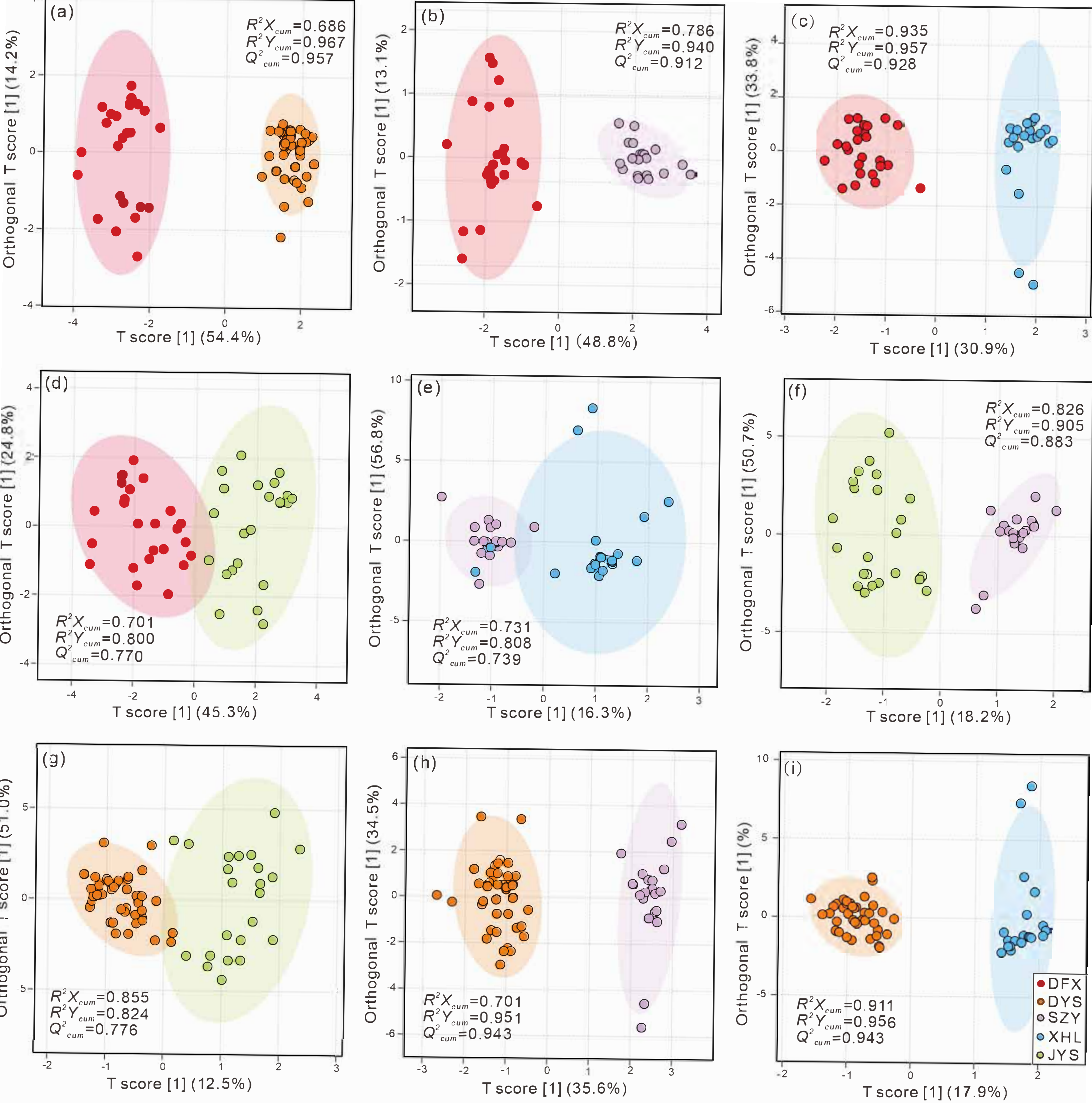
(a)
R^2X_{cum}=0.686
R^2Y_{cum}=0.967
Q^2_{cum}=0.957
Orthogonal T score [1] (14.2%)
T score [1] (54.4%)
(b)
R^2X_{cum}=0.786
R^2Y_{cum}=0.940
Q^2_{cum}=0.912
Orthogonal T score [1] (13.1%)
T score [1] (48.8%)
(c)
R^2X_{cum}=0.935
R^2Y_{cum}=0.957
Q^2_{cum}=0.928
Orthogonal T score [1] (33.8%)
T score [1] (30.9%)
(d)
R^2X_{cum}=0.701
R^2Y_{cum}=0.800
Q^2_{cum}=0.770
Orthogonal T score [1] (24.8%)
T score [1] (45.3%)
(e)
R^2X_{cum}=0.731
R^2Y_{cum}=0.808
Q^2_{cum}=0.739
Orthogonal T score [1] (56.8%)
T score [1] (16.3%)
(f)
R^2X_{cum}=0.826
R^2Y_{cum}=0.905
Q^2_{cum}=0.883
Orthogonal T score [1] (50.7%)
T score [1] (18.2%)
(g)
R^2X_{cum}=0.855
R^2Y_{cum}=0.824
Q^2_{cum}=0.776
T score [1] (12.5%)
(h)
R^2X_{cum}=0.701
R^2Y_{cum}=0.951
Q^2_{cum}=0.943
Orthogonal T score [1] (34.5%)
T score [1] (35.6%)
(i)
R^2X_{cum}=0.911
R^2Y_{cum}=0.956
Q^2_{cum}=0.943
Orthogonal T score [1] (%)
T score [1] (17.9%)
DFX
DYS
SZY
XHL
JYS

Figure 13

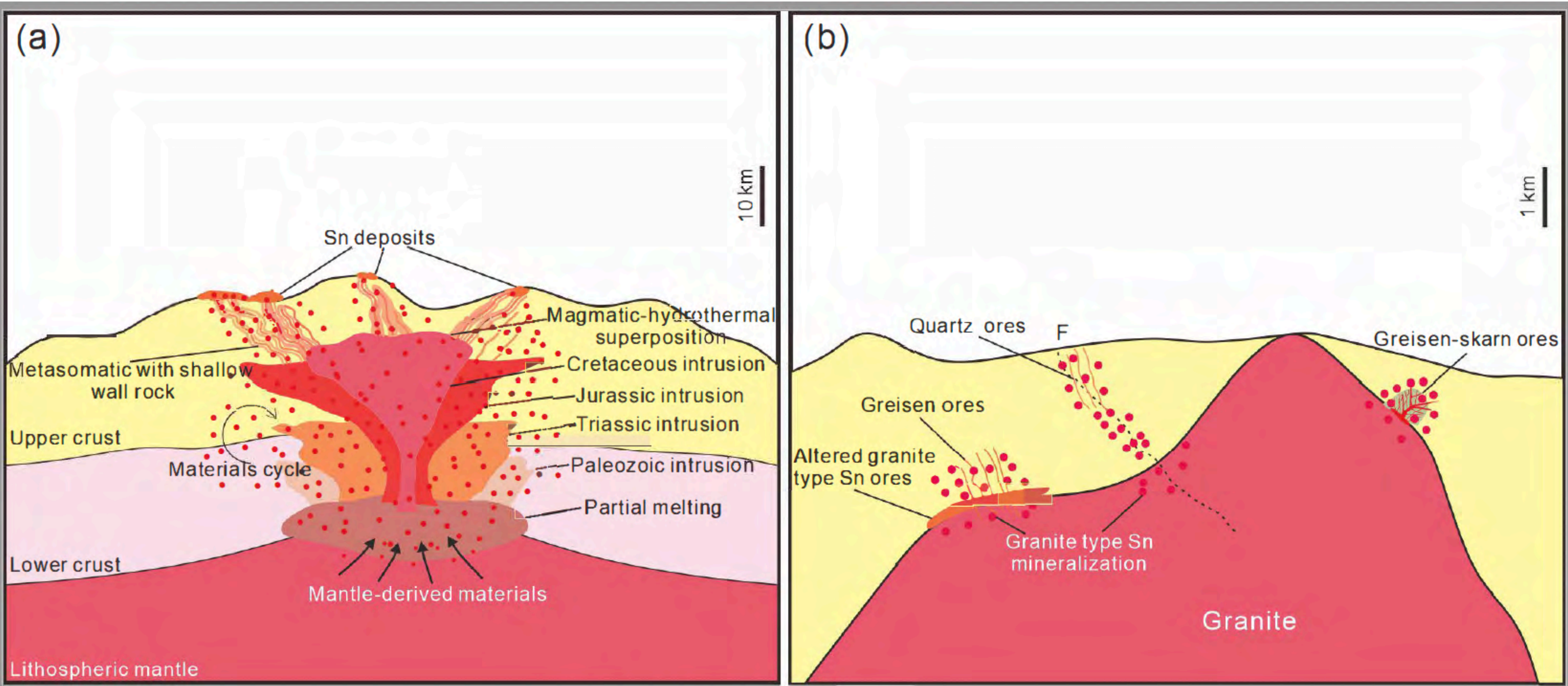
(a)
10 km
Sn deposits
Magmatic-hydrothermal superposition
Metasomatic with shallow wall rock
Cretaceous intrusion
Jurassic intrusion
Triassic intrusion
Upper crust
Materials cycle
Paleozoic intrusion
Partial melting
Lower crust
Mantle-derived materials
Lithospheric mantle
(b)
1 km
Quartz ores
F
Greisen-skarn ores
Greisen ores
Altered granite type Sn ores
Granite type Sn mineralization
Granite

Figure 14